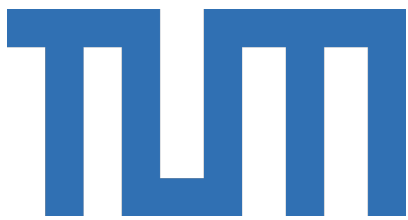


TECHNISCHE UNIVERSITÄT MÜNCHEN

LUDWIG-MAXIMILIANS-UNIVERSITÄT MÜNCHEN



Fermionic Gaussian State Assisted DMRG for 2D Hubbard Models

DMRG für 2D-Hubbard-Modelle mit Fermionischem
Gauß-Zustand

Guillermo Muñoz Menés

Master Thesis

M.Sc. Quantum Science and Technology

Supervisor: Prof. Dr. Jan von Delft

Co-supervisor: Prof. Dr. Hong-Hao Tu

I confirm that this Master Thesis in M.Sc. Quantum Science and Technology is my own work and I have documented all sources and material used.

Ich versichere, dass ich diese Master Thesis in M.Sc. Quantum Science and Technology selbstständig verfasst und nur die angegebenen Quellen und Hilfsmittel verwendet habe.

Munich, 01/10/2024

Guillermo Muñoz Menés

Acknowledgments

I would like to begin by expressing my sincere gratitude to Hong-Hao Tu for his invaluable insights and guidance throughout my thesis journey. I particularly appreciate his constant availability, always ready to help whenever I encountered challenges, while also granting me the independence to make progress on my own. He has been an exemplary mentor, offering support not only for thesis-related matters but also for a variety of other academic topics.

Heartfelt thanks go to Jan von Delft, who accepted me as his Master's student for this project. He introduced me to the captivating world of tensor networks, which has ultimately become my chosen research direction. His insightful discussions have been immensely helpful in shaping this thesis and guiding my research.

I also want to acknowledge the current and former members of the group with whom I shared this past year, especially Markus Scheb and Andreas Gleis, who assisted me with various aspects of the implementation, as well as Toni Guthardt and Mathias Pelz, who supported me with practical aspects of operational tasks within the group.

I would like to thank my environment in daily life, especially Ester, Zoe, and Pietro. Their invaluable emotional support and attention to my mental well-being have made some of the most stressful moments much easier to navigate. Without them, writing this thesis would have been significantly tougher.

Finally, my deepest gratitude is reserved for my parents and sister. Their unwavering support and guidance throughout my life have been instrumental in my journey. Despite being over 1000 km away, they have consistently succeeded in making me feel at home wherever I am. I owe everything I am to them.

Fermionic Gaussian State Assisted DMRG for 2D Hubbard Models

Abstract:

The Density Matrix Renormalization Group (DMRG) algorithm is one of the most widely used and successful numerical techniques for determining ground states in quantum systems. DMRG requires an initial state in Matrix Product State (MPS) form, and the choice of this initial state can significantly impact both the computational efficiency and the likelihood of finding the true ground state by avoiding local minima. In this thesis, we investigate the effect of using a fermionic Gaussian state as the initial ansatz for DMRG. Fermionic Gaussian states are advantageous because they are fully characterized by their covariance matrix, which scales quadratically with the system size. Previous studies have already demonstrated the benefit of using fermionic Gaussian states when exploring topologically ordered systems. In this thesis, we focus on the study of the 2D Hubbard model, and we explain how to implement an algorithm that gets a fermionic Gaussian state approximation of the ground state, converts it into an MPS, and initiates DMRG with it. We evaluate the performance of this approach by comparing it to the more conventional use of a product state as the initial ansatz. Our analysis covers both the half-filling case and the 1/8-hole-doping scenario. The results show that, for most parameter sets, the fermionic Gaussian state does not outperform the product state. However, in one of the 1/8-hole-doping cases, the Gaussian state successfully avoids a local minimum in which the product state becomes trapped, suggesting its potential advantage in specific situations.

Contents

Introduction	1
1. Theoretical Background	3
1.1. Physical model	3
1.1.1. Hubbard model	4
1.2. Fermionic Gaussian states	5
1.2.1. Majorana operators	6
1.2.2. Grassmann algebra	6
1.2.3. Definition of Gaussian states and the covariance matrix	7
1.2.4. Wick's theorem	8
1.2.5. Quadratic Hamiltonians	8
1.3. Tensor networks basics	10
1.3.1. Matrix Product States	10
1.3.2. Matrix Product Operators	13
1.3.3. Density Matrix Renormalization Group	14
2. Method: State initialization	17
2.1. Generalized Hartree-Fock Theory	17
2.1.1. Ground state search	17
2.2. MPS conversion of Gaussian states	20
2.2.1. Covariance matrix with vanishing off-diagonal terms	20
2.2.2. General case	22
2.3. Description of the algorithm	25
3. Numerical results	29
3.1. Benchmarks for the initial fermionic Gaussian state MPS obtention	29
3.2. Comparison of the DMRG performance	31
3.2.1. Half-filling case	31
3.2.2. Hole-doping case	37
4. Summary and outlook	45
A. Numerical implementation of the Bloch-Messiah decomposition	47
Bibliography	49

Introduction

In condensed matter physics, determining the ground state, the configuration of the system with the lowest possible energy, is a fundamental task. At zero temperature, the ground state represents the most stable arrangement of particles within the system and is crucial for understanding its overall behavior. The properties of the ground state dictate the quantum phase of the material, influencing whether it exhibits characteristics of a magnet, Mott insulator, conductor, or other phases.

While determining the ground state is of critical importance, finding an analytical solution to this problem is typically far from trivial. Many-body quantum systems, especially those with strong interactions, often lack known exact analytical solutions. As a result, numerical methods are frequently used to obtain an approximation to the ground state.

One of the most powerful and widely-used numerical techniques for this purpose is the Density Matrix Renormalization Group (DMRG) algorithm. Originally developed by Steven R. White in 1992 [1], DMRG has revolutionized the study of low-dimensional quantum systems. The algorithm relies on tensor network techniques to iteratively optimize the system's wave function, allowing for an efficient representation of the ground state even in systems where traditional methods struggle. In spite of its huge success for one-dimensional systems, DMRG has found some limitations when moving towards higher dimensional systems due to the increase in the computational resources required to successfully encode the relevant physics of the ground state. In order to try and mitigate this cost increment, further efforts to improve its performance have been made throughout the years [2–5].

The initial ansatz used to start the DMRG algorithm can significantly impact the method's overall success. This is because DMRG can get trapped to local minima if the initial state is not suitable. One of the reasons for this is that DMRG conserves the quantum numbers of the initial state during its iterative updates. As a result, to accurately obtain the system's true ground state and avoid convergence to a local minimum, it is a necessary condition (though not sufficient) that the initial state shares the same quantum numbers as the target ground state.

The primary objective of this thesis is to explore the effectiveness of using a good approximation of the true ground state as the initial state in DMRG computations. The goal is to improve overall performance by either reducing computation time or minimizing the likelihood of converging to a local minimum.

Previous research demonstrated the benefits of employing Gutzwiller-projected fermionic Gaussian states to initialize DMRG when studying topologically ordered systems [6], a strategy that was subsequently adopted in several studies [7–10].

In our case, we will study the use of a fermionic Gaussian state approximation to the ground state as the initial ansatz for DMRG. Fermionic Gaussian states are characterized by a density matrix that can be expressed as a quadratic function of canonical creation and annihilation operators, and they are fully described by their covariance matrix [11, 12]. Unlike arbitrary states, where the number of elements

grows exponentially with the system size, the covariance matrix for Gaussian states scales quadratically, making them particularly suitable for numerical calculations. A ground state approximation for interacting Hamiltonians can be obtained by performing successive short imaginary time evolutions and projecting the results onto the set of Gaussian states at each step [13].

The DMRG performance will be tested on the Hubbard model, a fundamental model in condensed matter physics that has attracted significant interest since it was first introduced by John Hubbard [14]. The Hubbard model provides a framework to study the interplay between electron hopping, which allows electrons to move between neighboring lattice sites, and an on-site electron-electron interaction, which accounts for the energy cost of having two electrons occupy the same site. Despite its apparent simplicity, the Hubbard model exhibits a rich phase diagram, including metallic, Mott insulating, and magnetically ordered phases [15]. Due to the presence of a quartic interaction term, finding an analytical solution for an arbitrary choice of the model's parameters is highly non-trivial. Consequently, the Hubbard model has been extensively studied by a wide range of numerical techniques [16–22].

In Chapter 1, we introduce the theoretical background essential for comprehending the motivation and functionality of the proposed method. This chapter covers several key topics, including an explanation of the Hubbard model, a definition of Gaussian states, and a brief introduction to fundamental concepts in tensor networks, with a particular focus on the DMRG algorithm.

Chapter 2 describes the method to obtain the Matrix Product State (MPS) used to initialize DMRG. We begin by explaining how to obtain a fermionic Gaussian state approximation of the real ground state through an imaginary time evolution. Then, we will describe how to convert the resulting state into an MPS starting uniquely from its covariance matrix. Finally, we include an step-by-step description of how the full algorithm was implemented.

In Chapter 3, we present our numerical results. We start by showing some benchmarks on the obtention of the initial fermionic Gaussian state MPS. Afterwards, we show the DMRG performance comparison considering two possible scenarios: half-filling and 1/8-hole-doping. The main metrics considered for the comparison are the computational time required and the energy reached by the DMRG converged states.

To conclude, Chapter 4 provides a summary of our work, the main conclusions obtained after evaluating the results, and some proposals for further research.

In Appendix A, the interested reader can find some details on the numerical implementation of the Bloch-Messiah decomposition, one of the fundamental steps for compressing a fermionic Gaussian state into an MPS.

1. Theoretical Background

In this chapter, we begin by briefly summarizing the physics of fermions and introducing the physical model that will be of interest for benchmarking our method: the Hubbard model.

In Sec. 1.2, we will introduce Gaussian states and their advantage for performing numerical calculations.

In Sec. 1.3, a brief overview of the basic tensor network building blocks, as well as our variational ground state search algorithm, will be provided.

1.1. Physical model

During this thesis, we will focus on the study of interacting fermions in a lattice. Before introducing the model that will govern the dynamics of our particles, it is convenient to set up the physical and mathematical framework in which we will work.

Fermions are described in particle physics as particles with half-integer spin that obey Pauli's exclusion principle and, therefore, obey Fermi-Dirac statistics. In our case, we will restrict ourselves to spin-1/2 particles. In order to work with such particles, we need to define their corresponding creation and annihilation operators. Opposed to their bosonic counterpart, those operators are not introduced in terms of position and momentum operators but in terms of their action on the vacuum state. Therefore, we define the creation operator \hat{a}_σ^\dagger as the operator that generates a fermion with magnetic quantum number m_s equal to σ and, analogously, the annihilation operator \hat{a}_σ as the operator that annihilates a fermion with magnetic quantum number m_s equal to σ :

$$\hat{a}_\sigma^\dagger |0\rangle = \begin{cases} |\uparrow\rangle & \text{if } \sigma = 1/2 \\ |\downarrow\rangle & \text{if } \sigma = -1/2 \end{cases}, \quad \hat{a}_{\sigma'} \hat{a}_\sigma^\dagger |0\rangle = \delta_{\sigma,\sigma'} |0\rangle, \quad (1.1.1)$$

where we have defined $|\uparrow\rangle := |S = 1/2, m_s = 1/2\rangle$, $|\downarrow\rangle := |S = 1/2, m_s = -1/2\rangle$ and where $|0\rangle$ represents the vacuum state, characterized by being annihilated by any annihilation operator, i.e., $\hat{a}_\sigma |0\rangle = 0 \forall \sigma$.

These operators are defined to satisfy the so-called canonical anticommutation relations (CARs). If we consider an ensemble of sites instead of a single one, these relations can be expressed as

$$\{\hat{a}_{i,\sigma}, \hat{a}_{j,\sigma'}^\dagger\} = \delta_{i,j} \delta_{\sigma,\sigma'}, \quad \{\hat{a}_{i,\sigma}, \hat{a}_{j,\sigma'}\} = \{\hat{a}_{i,\sigma}^\dagger, \hat{a}_{j,\sigma'}^\dagger\} = 0, \quad (1.1.2)$$

where $\{\hat{A}, \hat{B}\} := \hat{A}\hat{B} + \hat{B}\hat{A}$. The CARs ensure that the fermions satisfy the Pauli principle ($\hat{a}_{i,\sigma}^\dagger \hat{a}_{i,\sigma}^\dagger |0\rangle = -\hat{a}_{i,\sigma}^\dagger \hat{a}_{i,\sigma}^\dagger |0\rangle \rightarrow \hat{a}_{i,\sigma}^\dagger \hat{a}_{i,\sigma}^\dagger |0\rangle = 0$) and that the system's wave function changes sign under the exchange of two fermions with different label. Additionally, the CARs also require us to establish a convention when defining states.

That is, for example, that state $|\dots \uparrow_i \dots \uparrow_j \dots\rangle$ could be represented as both $\hat{a}_{i,\uparrow}^\dagger \hat{a}_{j,\uparrow}^\dagger |0\rangle$ or $\hat{a}_{j,\uparrow}^\dagger \hat{a}_{i,\uparrow}^\dagger |0\rangle$ which differ by a sign. In our work, we will define the Fock basis as

$$|n_{1,\uparrow}, n_{1,\downarrow}, n_{2,\uparrow}, \dots, n_{N,\uparrow}, n_{N,\downarrow}\rangle = (\hat{a}_{1,\uparrow}^\dagger)^{n_{1,\uparrow}} (\hat{a}_{1,\downarrow}^\dagger)^{n_{1,\downarrow}} (\hat{a}_{2,\uparrow}^\dagger)^{n_{2,\uparrow}} \dots (\hat{a}_{N,\uparrow}^\dagger)^{n_{N,\uparrow}} (\hat{a}_{N,\downarrow}^\dagger)^{n_{N,\downarrow}} |0\rangle \quad (1.1.3)$$

with N the total number of sites and $n_{i,\sigma}$ the number of fermions with spin σ in site i .

1.1.1. Hubbard model

The Hubbard model is one of the most well-known models for describing interacting fermions in a lattice. In the computations performed in this thesis and for this theoretical introduction, we will restrict ourselves to the study of square lattices. The model can be used to understand how such interactions can give rise to Mott insulating and magnetic effects in a solid. Due to the Pauli principle, each site has local dimension 4, corresponding to the following possible configurations: completely empty $|0\rangle$, occupied by a single spin-up fermion $|\uparrow\rangle$, occupied by a single spin-down fermion $|\downarrow\rangle$ and completely occupied $|\uparrow\downarrow\rangle$.

The model can be understood intuitively by considering the motion of fermions in a lattice. First, we may think about the kinetic energy. For that, it seems reasonable to consider a term that destroys a fermion in one site and creates it in another. This hopping term is modulated by an energy scale that we will denote as t . Additionally, fermions interact with each other through a screened Coulomb interaction. As that interaction decays with the distance between particles, we can approximate it to only have a non-vanishing effect for particles occupying the same site, in which case they would interact with an energy U (Fig. 1.1). In addition, we can include a chemical potential term μ . A Hamiltonian describing such behavior can be written as

$$\hat{H} = -t \sum_{\langle i,j \rangle, \sigma} \left(\hat{a}_{i,\sigma}^\dagger \hat{a}_{j,\sigma} + \hat{a}_{j,\sigma}^\dagger \hat{a}_{i,\sigma} \right) + U \sum_i \left(\hat{n}_{i,\uparrow} - \frac{1}{2} \right) \left(\hat{n}_{i,\downarrow} - \frac{1}{2} \right) - \mu \sum_{i,\sigma} \hat{n}_{i,\sigma}, \quad (1.1.4)$$

where $\langle i, j \rangle$ indicates that the sum extends only to nearest-neighbor sites and $\hat{n}_{i,\sigma} := \hat{a}_{i,\sigma}^\dagger \hat{a}_{i,\sigma}$ is the number operator. From the Hamiltonian, we can distinguish the kinetic energy term,

$$\hat{H}_t = -t \sum_{\langle i,j \rangle, \sigma} \left(\hat{a}_{i,\sigma}^\dagger \hat{a}_{j,\sigma} + \hat{a}_{j,\sigma}^\dagger \hat{a}_{i,\sigma} \right), \quad (1.1.5)$$

the interaction term,

$$\hat{H}_U = U \sum_i \left(\hat{n}_{i,\uparrow} - \frac{1}{2} \right) \left(\hat{n}_{i,\downarrow} - \frac{1}{2} \right), \quad (1.1.6)$$

and the chemical potential term,

$$\hat{H}_\mu = -\mu \sum_{i,\sigma} \hat{n}_{i,\sigma}. \quad (1.1.7)$$

Some additional interesting properties of the model are its symmetries. The Hub-

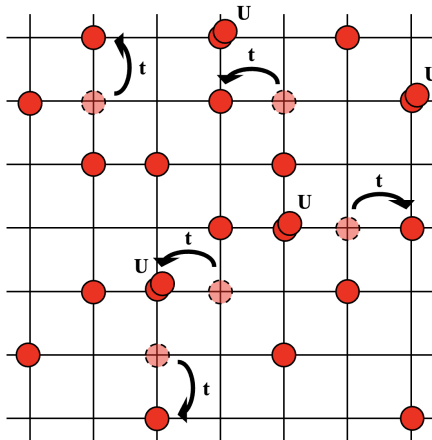


Figure 1.1.: Graphic representation of the kinetic and interaction terms of the Hubbard model on a square lattice.

bard Hamiltonian shows a conservation in the total particle number of the system. In the absence of an external magnetic field, it also remains invariant under a spin rotation transformation. Those correspond to a $U(1)$ and $SU(2)$ symmetry, respectively. Additionally, let's consider the particle-hole transformation

$$\hat{a}_{i,\sigma} \rightarrow (-1)^i \hat{a}_{i,\sigma}^\dagger. \quad (1.1.8)$$

Under such a transformation, both the kinetic \hat{H}_t and the interaction \hat{H}_U terms of the Hamiltonian remain unchanged. Therefore, the only term that would be affected is the chemical potential one \hat{H}_μ . That is, the total Hamiltonian will be modified as

$$\hat{H}_t + \hat{H}_U + \hat{H}_\mu \rightarrow \hat{H}_t + \hat{H}_U - \hat{H}_\mu - 2\mu N \quad (1.1.9)$$

with N the total number of sites. It is then easy to see from Eq. (1.1.9) that for $\mu = 0$, corresponding to the half-filling case [23], the Hamiltonian presents a particle-hole symmetry which implies that the phase diagram of the Hubbard Hamiltonian is symmetric around this half-filling configuration.

To conclude, we will briefly discuss some of the expected ground state configurations in a square lattice. For repulsive interactions ($U > 0$), one expects the state to be in an antiferromagnetic ground state, and for large values of U , the system is expected to behave as if it was governed by a Heisenberg Hamiltonian. On the other hand, for attractive ($U < 0$) and large interactions, we expect pairs of opposite spin fermions to form a singlet on a site [24].

1.2. Fermionic Gaussian states

Following the procedure presented in Ref. [11], we introduce Gaussian states and the formalism required to define them.

1.2.1. Majorana operators

The fermionic creation and annihilation operators introduced in Eq. (1.1.1) are usually known as Dirac operators and are not Hermitian. However, if we consider n fermionic modes, we can define a Hermitian combination of those operators that receive the name of Majorana operators:

$$\hat{c}_{2j-1} = \frac{1}{\sqrt{2}} (\hat{a}_j^\dagger + \hat{a}_j), \quad \hat{c}_{2j} = \frac{-i}{\sqrt{2}} (\hat{a}_j^\dagger - \hat{a}_j). \quad (1.2.1)$$

It can be shown from Eq. (1.1.2) that Majorana operators satisfy the Clifford algebra \mathcal{C}_{2n}

$$\{\hat{c}_j, \hat{c}_k\} = 2\delta_{jk} \quad \forall 1 \leq j, k \leq 2n. \quad (1.2.2)$$

Furthermore, they are traceless and any arbitrary element $\hat{X} \in \mathcal{C}_{2n}$ can be expressed as a polynomial of Majorana operators:

$$\hat{X} = \alpha \hat{\mathbb{1}} + \sum_{p=1}^{2n} \sum_{1 \leq j_1 < \dots < j_p \leq 2n} \alpha_{j_1, \dots, j_p} \hat{c}_{j_1} \dots \hat{c}_{j_p} \quad (1.2.3)$$

with $\alpha, \alpha_{j_1, \dots, j_p} \in \mathbb{R}$. The parameter α is related to the trace of operator \hat{X}

$$\alpha = \frac{1}{2^n} \text{Tr}[\hat{X}]. \quad (1.2.4)$$

A particularly interesting operator is the parity operator

$$\hat{P} = \prod_{i=1}^N \prod_{\sigma \in \{\uparrow, \downarrow\}} (\hat{\mathbb{1}} - 2\hat{a}_{i,\sigma}^\dagger \hat{a}_{i,\sigma}) = i^{2n} \hat{c}_1 \hat{c}_2 \dots \hat{c}_{2n}, \quad (1.2.5)$$

where N is the number of sites. We say that an operator \hat{X} is even (odd) if $\hat{P}\hat{X} = (-)\hat{X}$ or, analogously, if it involves only even (odd) powers of Majorana operators.

1.2.2. Grassmann algebra

Before properly defining Gaussian states, allow us to introduce Grassmann variables and their algebra. Consider an n -dimensional complex linear space \mathbb{C}^n and its basis vectors $\theta_1, \dots, \theta_n$. Grassmann algebra with complex coefficients \mathcal{G}_n is generated by formal variables $\theta_1, \dots, \theta_n$ subject to the following multiplication rules:

$$\theta_j^2 = 0, \quad \{\theta_j, \theta_k\} = 0 \quad \forall 1 \leq j, k \leq n. \quad (1.2.6)$$

An arbitrary element $f \in \mathcal{G}_n$ can be expressed as a polynomial of Grassmann variables

$$f(\theta) = \alpha + \sum_{p=1}^n \sum_{1 \leq j_1 < \dots < j_p \leq n} \alpha_{j_1, \dots, j_p} \theta_{j_1} \dots \theta_{j_p}, \quad (1.2.7)$$

where we have defined $\theta := (\theta_1, \dots, \theta_n)$.

Partial derivatives of Grassmann variables are linear operators

$$\frac{\partial}{\partial \theta_j} : \mathcal{G}_n \rightarrow \mathcal{G}_n \quad (1.2.8)$$

defined by

$$\frac{\partial}{\partial \theta_j} 1 = 0, \quad \frac{\partial}{\partial \theta_j} \theta_k = \delta_{jk}, \quad (1.2.9)$$

and by the Leibniz's rule

$$\frac{\partial}{\partial \theta_j} (\theta_k f(\theta)) = \delta_{jk} f(\theta) - \theta_k \frac{\partial}{\partial \theta_j} f(\theta). \quad (1.2.10)$$

Since the derivative $\frac{\partial}{\partial \theta_j} f(\theta)$ no longer depends on θ_j , we can define integration as a linear operator that acts as a derivative and maps \mathcal{G}_n into \mathcal{G}_{n-1} , i.e.,

$$\int d\theta_j := \frac{\partial}{\partial \theta_j} : \mathcal{G}_n \rightarrow \mathcal{G}_{n-1}. \quad (1.2.11)$$

One interesting property of Grassmann variables is that one can map any polynomial of Majorana operators to a polynomial $\omega(\hat{c}_{j_1} \hat{c}_{j_2} \dots \hat{c}_{j_p}, \theta)$ of $2n$ Grassmann variables

$$\omega(\hat{c}_{j_1} \hat{c}_{j_2} \dots \hat{c}_{j_p}, \theta) = \theta_{j_1} \theta_{j_2} \dots \theta_{j_p} \quad (1.2.12)$$

$$\omega(\hat{\mathbb{1}}_{2n \times 2n}, \theta) = 1. \quad (1.2.13)$$

Since any operator \hat{X} , can be expressed as a polynomial of Majorana operators (Eq. (1.2.3)), one can also assign a polynomial of Grassmann variables to any operator $\omega(\hat{X}, \theta)$, which receives the name of Grassmann representation of \hat{X} . It is interesting to emphasize that ω is just an isomorphism between spaces and is not related to a multiplication in the algebras \mathcal{C}_{2n} and \mathcal{G}_{2n} .

1.2.3. Definition of Gaussian states and the covariance matrix

Definition 1.1. A quantum state of n fermionic modes is Gaussian iff its density operator ρ has a Gaussian Grassmann representation [11]

$$\omega(\rho, \theta) = \frac{1}{2^n} \exp\left(\frac{i}{2} \theta^T \Gamma \theta\right) \quad (1.2.14)$$

for some $2n \times 2n$ real antisymmetric matrix Γ and $\theta := (\theta_1, \dots, \theta_{2n})^T$. The matrix Γ is called a covariance matrix of ρ .

The covariance matrix can be found to be

$$\Gamma_{jk} = \frac{i}{2} \text{Tr}(\rho[\hat{c}_j, \hat{c}_k]) = \begin{cases} i \text{Tr}(\rho \hat{c}_j \hat{c}_k) & \text{for } j \neq k \\ 0 & \text{for } j = k \end{cases} \quad (1.2.15)$$

Γ is the covariance matrix of a physical state iff $i\Gamma - \hat{\mathbb{1}} \leq 0$, while pure states have to fulfill $\Gamma^2 = -\hat{\mathbb{1}}$ [13].

The covariance matrix can also be represented in the Dirac representation, in which case we define it as

$$\Gamma^{\text{dir}} = \left(\begin{array}{cc} \langle \hat{a}_j^\dagger \hat{a}_i \rangle & \langle \hat{a}_j \hat{a}_i \rangle \\ \langle \hat{a}_j^\dagger \hat{a}_i^\dagger \rangle & \langle \hat{a}_j \hat{a}_i^\dagger \rangle \end{array} \right)_{1 \leq i, j \leq n}, \quad (1.2.16)$$

where $\langle \hat{X} \rangle$ is the expectation value of the operator \hat{X} for a system that is in a state ρ , and is defined as $\langle \hat{X} \rangle := \text{Tr}(\rho \hat{X})$.

By defining a unitary $2n \times 2n$ transformation

$$\Omega = \left(\begin{array}{cccc|cccc} 1 & 0 & \cdots & 0 & 1 & 0 & \cdots & 0 \\ i & 0 & \cdots & 0 & -i & 0 & \cdots & 0 \\ 0 & 1 & \cdots & 0 & 0 & 1 & \cdots & 0 \\ 0 & i & \cdots & 0 & 0 & -i & \cdots & 0 \\ \vdots & \vdots & \ddots & \vdots & \vdots & \vdots & \ddots & \vdots \\ 0 & 0 & \cdots & 1 & 0 & 0 & \cdots & 1 \\ 0 & 0 & \cdots & i & 0 & 0 & \cdots & -i \end{array} \right) \quad (1.2.17)$$

such that $\vec{c} = \Omega \vec{\alpha}$ with $\vec{c} = (\hat{c}_1, \dots, \hat{c}_{2n})^T$ and $\vec{\alpha} = (\hat{a}_1, \dots, \hat{a}_n, \hat{a}_1^\dagger, \dots, \hat{a}_n^\dagger)^T$, we can change between the two possible covariance matrix representations as [12]

$$\Gamma = -i\Omega (2\Gamma^{\text{dir}} - \hat{1}) \Omega^\dagger. \quad (1.2.18)$$

1.2.4. Wick's theorem

One of the most interesting properties of Gaussian states is that they satisfy the Wick's theorem which can be expressed in terms of the covariance matrix as

$$i^p \text{Tr}(\rho \hat{c}_{j_1} \dots \hat{c}_{j_{2p}}) = \text{Pf}(\Gamma|_{j_1 \dots j_{2p}}) \quad \text{with } 1 \leq j_1 < \dots < j_{2p} \leq 2n, \quad (1.2.19)$$

where $\Gamma|_{j_1 \dots j_{2p}}$ is the $2p \times 2p$ submatrix of Γ that results from taking the rows and columns of the corresponding indices j_α and $\text{Pf}(\Gamma|_{j_1 \dots j_{2p}})^2 = \det(\Gamma|_{j_1 \dots j_{2p}})$ is called the Pfaffian.

By combining Wick's theorem with the fact that every operator can be expressed as a polynomial of Majorana operators, it becomes clear that all higher-order correlations of a Gaussian state can be derived from its covariance matrix. Consequently, a Gaussian state is fully characterized by its covariance matrix. This has a significant implication: for a lattice of N sites with local dimension d , only $O(N^2)$ elements are needed to describe a Gaussian state, in contrast to the $O(d^N)$ elements required to describe a general state. The reduced number of elements necessary to specify the state makes Gaussian states particularly well-suited for numerical calculations.

1.2.5. Quadratic Hamiltonians

Fermionic Gaussian states are tightly related to the study of quadratic Hamiltonians. The most general quadratic Hamiltonian can be written in the Dirac representation

as

$$\hat{H} = \sum_{i,j=1}^n t_{ij} \hat{a}_i^\dagger \hat{a}_j + \frac{1}{2} \sum_{i,j=1}^n \left(\Delta_{ij} \hat{a}_i^\dagger \hat{a}_j^\dagger + \Delta_{ij}^* \hat{a}_i \hat{a}_j \right), \quad (1.2.20)$$

where the hermiticity of \hat{H} requires the matrix t to be hermitian ($t_{ij} = t_{ji}^*$) and the matrix Δ to be skew-symmetric ($\Delta_{ij} = -\Delta_{ji}$). Such a Hamiltonian can be more compactly represented in matrix form as

$$\hat{H} = \frac{1}{2} \vec{\alpha}^\dagger \mathcal{H} \vec{\alpha} + \frac{1}{2} \text{Tr}(t), \quad (1.2.21)$$

where we have defined $\vec{\alpha} = \left(\hat{a}_1, \dots, \hat{a}_n, \hat{a}_1^\dagger, \dots, \hat{a}_n^\dagger \right)^T$ and

$$\mathcal{H} = \begin{pmatrix} t & \Delta \\ -\Delta^* & -t^* \end{pmatrix}. \quad (1.2.22)$$

Similarly, a quadratic Hamiltonian can be written in terms of Majorana operators as

$$\hat{H} = i \sum_{i,j=1}^{2n} h_{ij} \hat{c}_i \hat{c}_j, \quad (1.2.23)$$

where h is a real and skew-symmetric matrix.

All Gaussian states remain Gaussian when evolving under the action of a quadratic Hamiltonian, and its covariance matrix evolves according to

$$\Gamma(t) = O(t) \Gamma(0) O(t)^T, \quad (1.2.24)$$

where $O(t) = e^{Aht}$ is an orthogonal transformation [13].

Additionally, every pure fermionic Gaussian state is the ground state of a quadratic Hamiltonian. In order to understand how to get the covariance matrix representing the ground state of a certain quadratic Hamiltonian we can start from noticing that the Hamiltonian matrix represented in Eq. (1.2.22) has a particle-hole symmetry, manifested by

$$\Sigma \mathcal{H} \Sigma = -\mathcal{H} \quad (1.2.25)$$

with

$$\Sigma = \begin{pmatrix} 0 & \mathbb{1}_{n \times n} \\ \mathbb{1}_{n \times n} & 0 \end{pmatrix} K, \quad (1.2.26)$$

where K performs the complex conjugation operation. Having that symmetry implies that the eigenvalues of \mathcal{H} are symmetric with respect to zero, i.e., one can always find a unitary transformation B

$$B = \begin{pmatrix} U & V^* \\ V & U^* \end{pmatrix} \quad (1.2.27)$$

such that

$$\mathcal{H} = B \begin{pmatrix} \Lambda & 0 \\ 0 & -\Lambda \end{pmatrix} B^\dagger \quad (1.2.28)$$

with $\Lambda_{ij} = \epsilon_i \delta_{ij}$ and $\epsilon_i \geq 0 \forall i = 1, \dots, n$. The matrix B receives the name of

Bogoliubov transformation.

We can then further develop Eq. (1.2.21) and obtain

$$\begin{aligned}\hat{H} &= \frac{1}{2}\bar{\alpha}^\dagger \mathcal{H} \bar{\alpha} + \frac{1}{2} \text{Tr}(t) = \frac{1}{2}\bar{\alpha}^\dagger B \begin{pmatrix} \Lambda & 0 \\ 0 & -\Lambda \end{pmatrix} B^\dagger \bar{\alpha} + \frac{1}{2} \text{Tr}(t) \\ &= \frac{1}{2}\bar{\delta}^\dagger \begin{pmatrix} \Lambda & 0 \\ 0 & -\Lambda \end{pmatrix} \bar{\delta} + \frac{1}{2} \text{Tr}(t),\end{aligned}\tag{1.2.29}$$

where we have defined new fermionic eigenmodes as $\bar{\delta} := (\hat{d}_1, \dots, \hat{d}_n, \hat{d}_1^\dagger, \dots, \hat{d}_n^\dagger)^T = B^\dagger \bar{\alpha}$. By using these eigenmodes, the Hamiltonian is brought into a diagonal form

$$\begin{aligned}\hat{H} &= \frac{1}{2} \sum_{i=1}^n (\epsilon_i \hat{d}_i^\dagger \hat{d}_i - \epsilon_i \hat{d}_i \hat{d}_i^\dagger) + \frac{1}{2} \text{Tr}(t) \\ &= \sum_{i=1}^n \epsilon_i \hat{d}_i^\dagger \hat{d}_i - \frac{1}{2} \sum_{i=1}^n \epsilon_i + \frac{1}{2} \text{Tr}(t).\end{aligned}\tag{1.2.30}$$

Since $\epsilon_i \geq 0$, the ground state will be the vacuum of d modes. By looking at Eq. (1.2.16), it is easy to see that the covariance matrix of such a state in the diagonal basis of eigenmodes is just

$$\Gamma^D = \begin{pmatrix} 0 & 0 \\ 0 & \hat{\mathbb{1}} \end{pmatrix}.\tag{1.2.31}$$

Finally, since the same unitary transformation that diagonalizes the Hamiltonian also diagonalizes the covariance matrix, we can recover the expression of the covariance matrix in terms of the original fermionic creation and annihilation modes as

$$\Gamma^{\text{dir}} = B \Gamma^D B^\dagger.\tag{1.2.32}$$

1.3. Tensor networks basics

Tensor network methods constitute one of the most relevant numerical techniques for efficiently encoding the information of both wave functions and the operators acting on them. Their main applications lie in the fields of quantum many-body physics, quantum information, and machine learning.

In this section, we will introduce the fundamentals of tensor networks and one of their most successful algorithms for ground state searching: the Density Matrix Renormalization Group (DMRG).

1.3.1. Matrix Product States

In quantum mechanics, all the information describing a state is encoded in its wave function. Given a lattice of N sites with local dimension d , a general state $|\psi\rangle$ is

determined by a tensor of $O(d^N)$ elements,

$$|\psi\rangle = \sum_{\sigma_1, \sigma_2, \dots, \sigma_N=1}^d T^{\sigma_1 \sigma_2 \dots \sigma_N} |\sigma_1\rangle |\sigma_2\rangle \dots |\sigma_N\rangle =: \sum_{\vec{\sigma}} T^{\vec{\sigma}} |\vec{\sigma}\rangle, \quad (1.3.1)$$

where we have defined $\vec{\sigma} := (\sigma_1, \sigma_2, \dots, \sigma_N)$.

Matrix Product States (MPSs) provide an alternative way to represent a quantum state using a set of tensors. These tensors are contracted through certain indices, referred to as bond indices:

$$|\psi\rangle = \sum_{\vec{\sigma}, \vec{\chi}} [M_1]_{\chi_1}^{1, \sigma_1} [M_2]_{\chi_2}^{\chi_1, \sigma_2} \dots [M_N]_1^{\chi_{N-1}, \sigma_N} |\vec{\sigma}\rangle. \quad (1.3.2)$$

where we have defined $\vec{\chi} := (\chi_1, \chi_2, \dots, \chi_{N-1})$. Each bond index χ_i will have a bond dimension D_i . If we define $D := \max(\{D_i\})$, the required number of elements to represent the state in MPS form is $O(ND^2d)$; see Fig. 1.2.

If we compare the required number of elements for both representations, we can notice that, as long as the maximum bond dimension D remains small (does not increase exponentially with the size of our system), the MPS representation offers an exponential advantage with respect to the conventional representation. Some notable examples where an exact MPS representation with small D is possible are product states ($D = 1$) and the entangled state $|GHZ\rangle$ ($D = d$).

In cases where an exact representation requires an exponentially increasing bond dimension, an efficient approximation can usually still be found via a truncation scheme. One of the simplest and most widely used truncation protocols consists of the following:

1. Starting from our initial tensor $T^{\vec{\sigma}}$ representing the state, we perform a singular value decomposition (SVD) as

$$T^{\sigma_1, \alpha} = \sum_{\chi_1, \chi'_1=1}^{D_1} U_{\chi_1}^{\sigma_1} S_{\chi'_1}^{\chi_1} V^{\dagger \chi'_1, \alpha}, \quad (1.3.3)$$

where $\alpha = (\sigma_2, \dots, \sigma_N)$ is a compound index and D_1 is the number of singular values.

2. Choose a maximum bond dimension $D < D_1$ and keep only the D largest

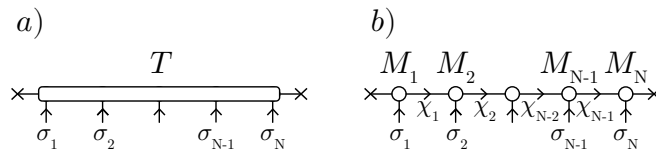


Figure 1.2.: Comparison between the conventional diagrammatic representation of (a) a state and (b) its MPS representation.

singular values and their corresponding left- and right-singular vectors.

$$T^{\sigma_1, \alpha} \approx \sum_{\chi_1, \chi'_1=1}^D \tilde{U}_{\chi_1}^{\sigma_1} \tilde{S}_{\chi'_1}^{\chi_1} \tilde{V}^{\dagger \chi'_1, \alpha}. \quad (1.3.4)$$

3. Define $M_1 := \tilde{U}$ and $T^{\sigma_2, \dots, \sigma_N} := \tilde{S} \tilde{V}^\dagger$.
4. Iterate through the steps with the new tensor T until reaching the MPS form of Eq. (1.3.2).

In addition to providing an effective representation of a state while keeping the required number of elements to describe it manageable, MPSs also offer an efficient contraction pattern when computing overlaps of the form

$$\begin{aligned} \langle \psi' | \psi \rangle &= \sum_{\vec{\sigma}, \vec{\sigma}', \vec{\chi}, \vec{\chi}'} [M_1^\dagger]_{1, \sigma'_1}^{\chi'_1} \dots [M_N^\dagger]_{\chi'_{N-1}, \sigma'_{N-1}}^1 [M_1]_{\chi_1}^{1, \sigma_1} \dots [M_N]_1^{\chi_{N-1}, \sigma_N} \langle \vec{\sigma}' | \vec{\sigma} \rangle \\ &= \sum_{\vec{\sigma}, \vec{\chi}, \vec{\chi}'} [M_1^\dagger]_{1, \sigma_1}^{\chi'_1} \dots [M_N^\dagger]_{\chi'_{N-1}, \sigma_N}^1 [M_1]_{\chi_1}^{1, \sigma_1} \dots [M_N]_1^{\chi_{N-1}, \sigma_N}. \end{aligned} \quad (1.3.5)$$

The contraction pattern consists of an iterative method following these steps:

1. Compute the element C_1 defined as

$$[C_1]_{\chi_1}^{\chi'_1} := \sum_{\sigma_1} [M_1^\dagger]_{1, \sigma_1}^{\chi'_1} [M_1]_{\chi_1}^{1, \sigma_1}. \quad (1.3.6)$$

2. Iteratively compute the elements

$$[C_l]_{\chi_l}^{\chi'_l} = \sum_{\chi'_{l-1}, \chi_{l-1}, \sigma_l} [C_{l-1}]_{\chi'_{l-1}}^{\chi'_{l-1}} [M_l^\dagger]_{\chi'_{l-1}, \sigma_l}^{\chi'_l} [M_l]_{\chi_l}^{\chi_{l-1}, \sigma_l}, \quad (1.3.7)$$

for each l .

3. Reach element $[C_N]_1^1$, which corresponds to the value of the desired overlap. A visual representation of the protocol can be found in Fig. 1.3.

To conclude this introduction on MPSs, it is worth mentioning that any product of matrices can be represented in infinitely many different ways without changing the final result:

$$MM' = (MU)(U^{-1}M') = \tilde{M}\tilde{M}', \quad (1.3.8)$$

with $\tilde{M} := MU$ and $\tilde{M}' := U^{-1}M'$. This Gauge freedom allows us to express the MPSs in particularly convenient ways, which receive the name of canonical forms. Those canonical forms exploit the usage of isometries: linear transformations that conserve the distance between points. A tensor A (B) is said to be left-(right-)normalized if it is a left (right) isometry, i.e., it satisfies $A^\dagger A = \mathbb{1}$ ($BB^\dagger = \mathbb{1}$).

One of the most used MPS representations is the so-called *site-canonical* form, which consists of the first $l - 1$ tensors being left isometries and the tensors from $l + 1$ to the last one being right isometries. The tensor in position l is the only one that is not an isometry and receives the name of orthogonality center.

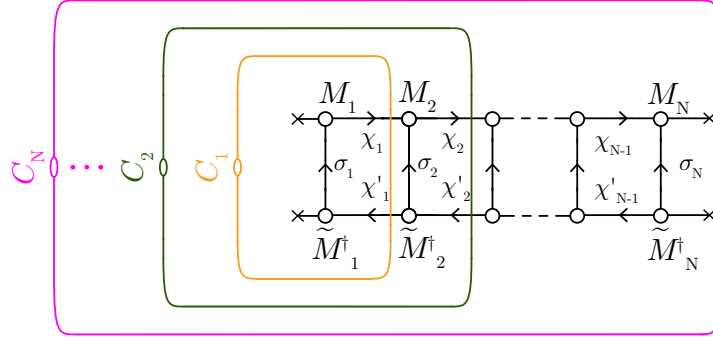


Figure 1.3.: Schematic representation of an efficient protocol for computing the overlap between two states represented in MPS form.

If the orthogonality center is in the first (last) position and the state is normalized, the orthogonality center is also a right (left) isometry. In that case, the MPS is said to be in *right-(left-)canonical* form.

One can also express the orthogonality center as $C_l = A_l S_l B_l$ where S_l is a diagonal matrix (e.g., through an SVD decomposition). Then, the MPS can be rewritten as $\dots A_{l-1} C_l B_{l+1} \dots = \dots A_{l-1} A_l S_l \tilde{B}_{l+1} \dots$ with $\tilde{B}_{l+1} := B_l B_{l+1}$ still being a right isometry. This new form of the MPS receives the name of *bond-canonical* form. A graphic representation of these canonical forms can be found in Fig. 1.4.

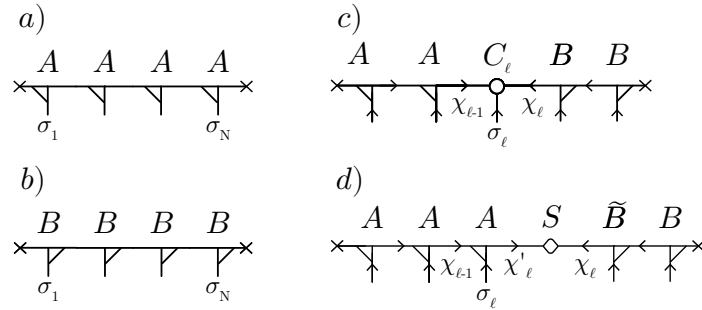


Figure 1.4.: Graphic representation of the canonical forms of an MPS: (a) *left-canonical*, (b) *right-canonical*, (c) *site-canonical*, (d) *bond-canonical*.

1.3.2. Matrix Product Operators

Following the same spirit of MPSs, we can define an specially convenient form for describing the action of the operators: Matrix Product Operators (MPOs). Conventionally, an operator that acts in a lattice of N sites with local dimension d will require $O(d^{2L})$ elements to be described:

$$\hat{O} = \sum_{\vec{\sigma}, \vec{\sigma}'} O_{\vec{\sigma}'}^{\vec{\sigma}} |\vec{\sigma}\rangle \langle \vec{\sigma}'|. \quad (1.3.9)$$

Alternatively, operators can also be described through an MPO,

$$\hat{O} = \sum_{\vec{\sigma}, \vec{\sigma}', \vec{\chi}} [W_1]_{\chi_1, \sigma'_1}^{1, \sigma_1} [W_2]_{\chi_2, \sigma'_2}^{\chi_1, \sigma_2} \dots [W_N]_{1, \sigma'_N}^{\chi_{N-1}, \sigma_N} |\vec{\sigma}\rangle \langle \vec{\sigma}'|. \quad (1.3.10)$$

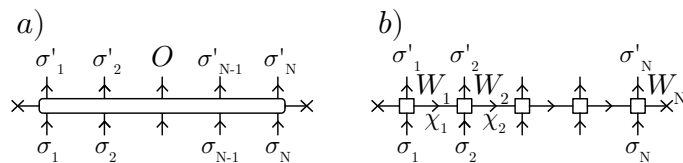


Figure 1.5.: Comparison between the conventional diagrammatic representation of (a) an operator and (b) its MPO representation.

The required number of elements to store the information of an MPO is $O(Nw^2d^2)$, where we have defined w as the maximum bond dimension (Fig. 1.5). In our case, we will be specially interested in the MPO of a certain Hamiltonian. For short-ranged Hamiltonians, a small value of w is typically enough to obtain an exact representation of its action.

One of the key advantages of using MPOs is their strong synergy with MPSs, since applying an MPO to an MPS produces a resulting state that remains in MPS form. Additionally, an analogous protocol to the one described to compute overlaps $\langle \psi' | \psi \rangle$ can be adopted to compute expected values $\langle \psi | \hat{O} | \psi \rangle$, as long as all the elements are on their corresponding MPS or MPO form.

1.3.3. Density Matrix Renormalization Group

The Density Matrix Renormalization Group (DMRG) is a highly successful and widely-used numerical method in the field of tensor networks. It is designed to iteratively search for the ground state of a given Hamiltonian. This method was originally developed by Steve R. White [1].

In order to perform a DMRG calculation, we need to start by obtaining the MPS and MPO representations of an initial state and the Hamiltonian, respectively. Now, we consider the space of all MPSs of a given bond dimension D as a variational space and the objective is to find the ground state, i.e. the state $|\psi\rangle$ that minimizes the energy,

$$E = \frac{\langle \psi | \hat{H} | \psi \rangle}{\langle \psi | \psi \rangle}. \quad (1.3.11)$$

Additionally, the normalization requirement adds an extra constraint into our minimization problem, which will be taken into account through a Lagrangian multiplier. Therefore, the quantity to be minimized is

$$\langle \psi | \hat{H} | \psi \rangle - \lambda \langle \psi | \psi \rangle. \quad (1.3.12)$$

A key insight of DMRG is its iterative approach to solving the optimization problem. The idea is to assume that all tensors in the MPS remain fixed, except for the one at position l . By optimizing the tensor at this position, a state with lower energy can be found, although it may not yet be the optimal ground state. The process then involves updating the tensor at site l with its variationally optimized version, moving to site $l + 1$, and treating that tensor as the one to be updated. This cycle is repeated until the energy no longer decreases when moving to a new site. The efficiency of the method is significantly enhanced by reshaping the MPS into a site-canonical form where the orthogonality center is aligned with the tensor being optimized.

Considering that the MPS is in site-canonical form, the detailed description of a single tensor update during a left-to-right sweep is

1. Set the minimization equation of Eq. (1.3.12) subject to the constraint of all tensors except from the one in site l , C_l , being constant:

$$\frac{\partial}{\partial C_l^\dagger} \left[\langle \psi | \hat{H} | \psi \rangle - \lambda \langle \psi | \psi \rangle \right] = 0, \quad (1.3.13)$$

2. Define an effective Hamiltonian $[\hat{H}^{(1)}]_a^{a'}$ such that Eq. (1.3.13) can be seen as an eigenvalue problem:

$$[\hat{H}^{(1)}]_a^{a'} [C_l]^a = \lambda [C_l]^{a'}, \quad (1.3.14)$$

where a and a' are composite indices.

This can be done partly thanks to the MPS being in site-canonical form with the orthogonality center in site l .

3. Solve the eigenvalue problem, get the eigenvector \tilde{C}_l with the lowest eigenvalue and substitute $C_l \rightarrow \tilde{C}_l$. The effective Hamiltonian is a matrix of $O(D^2 d \times D^2 d)$ elements, and therefore performing an exact diagonalization is typically non-convenient. As we are just interested in the eigenvector with the lowest eigenvalue, it is highly advisable to use a method that targets that eigenvalue, such as the Lanczos method [25].
4. Move the orthogonality center towards the next site, i.e., perform an SVD decomposition $\tilde{C}_l = USV^\dagger$ and redefine the MPS tensor in site l as $\tilde{A}_l := U$ and the one in site $l + 1$ as $C_{l+1} = SV^\dagger B_{l+1}$.

A graphic representation of some of the key elements of this update can be found in Fig. 1.6.

DMRG can be initialized with an arbitrary state far from the real ground state and, after enough iterations of the variational optimization process, the method will eventually converge to a certain energy value. However, the final state is not guaranteed to correspond to the real ground state. That is, DMRG has a probability to fall into local minima.

The protocol described in this section corresponds to a single-site update and it only considers the variational space of MPSs with a fixed bond dimension D . This implies, among other things, that if the initial state lies in a different symmetry sector than the true ground state, the one-site DMRG cannot expand the variational space to explore new symmetry sectors. As a result, the likelihood of converging to a local minimum is significant. To mitigate this risk, an alternative known as the two-site DMRG has been proposed, where the update involves two adjacent tensors simultaneously. This approach allows the method to increase the bond dimension D if necessary, enhancing accuracy and reducing the probability of getting trapped in a local minimum. However, the computational cost of the two-site update ($O(D^3 d^3 + D^3 d^2 w)$) is also considerably higher than that of the one-site update ($O(D^3 d w + D^2 d^2 w^2)$).

Alternative methods to increase the performance of one-site DMRG without increasing the computational cost to that of two-site DMRG by exploiting symmetries

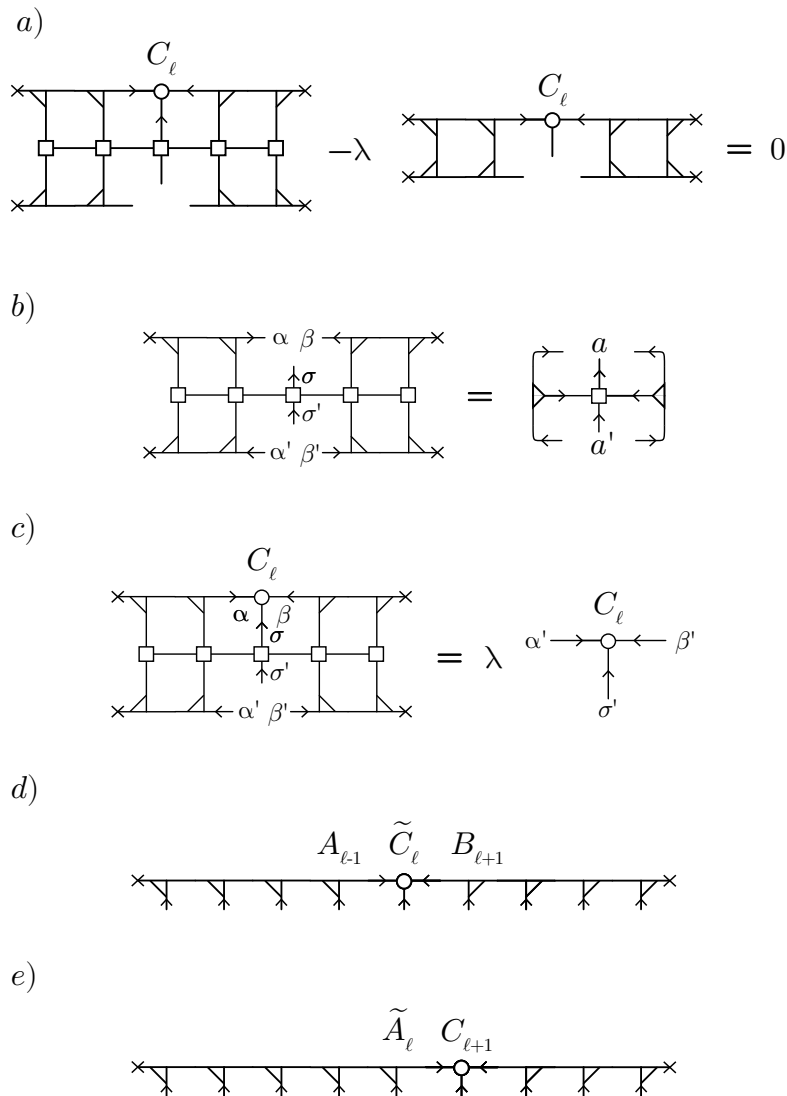


Figure 1.6.: Graphic representation of some of the elements used on the description of a single-site DMRG update. (a) Eq. (1.3.13), (b) effective Hamiltonian $[\hat{H}^{(1)}]_a^{a'}$ with $a = (\alpha, \sigma, \beta)$ and $a' = (\alpha', \sigma', \beta')$, (c) Eq. (1.3.14), (d) updated MPS, (e) MPS with shifted orthogonality center.

and quantum numbers have been suggested. Some of those are density matrix perturbation [2], the center matrix wave function formalism [3], subspace expansion [4] and controlled bond expansion (CBE) [5]. The results shown in Chapter 3 have been obtained via either two-site or CBE DMRG.

2. Method: State initialization

The main idea of this thesis is to develop a method to improve the performance of the DMRG algorithm by using a fermionic Gaussian state approximation of the real ground state as the initial variational ansatz.

During this chapter, we first describe how to get the best Gaussian state approximation to the ground state for a Hubbard-like model. Additionally, since the variational ansatz of the DMRG algorithm is an MPS, we also describe how to compress an arbitrary Gaussian state into its MPS form. To conclude, we introduce the implemented algorithm used to obtain the results shown in Chapter 3.

2.1. Generalized Hartree-Fock Theory

When studying the physics and the arising phenomena of many-body fermionic systems, the most well-known tools are Hartree-Fock and Bardeen, Cooper and Schrieffer (BCS) theory.

The usual Hartree-Fock theory for an N -particle system constitutes a mean-field theory approximation. It considers that the ground state can be approximated to a Slater determinant formed from N orthonormal, single-particle functions. One starts with a state of that shape and optimizes these single-particle functions to minimize the energy of the total state. The resulting state usually breaks some symmetries from the Hamiltonian, such as translation invariance. In BCS theory, a violation of the particle-number conservation is also permitted (even though parity is still preserved) as long as it allows us to reduce the energy [26].

These two theories can be unified under a more general one: the generalized Hartree-Fock theory. The key insight for doing so is realizing that both Hartree-Fock and BCS states belong to the family of fermionic Gaussian states, described in Sec. 1.2. In this section, we describe how to obtain the covariance matrix of the state that best approaches the real ground state of the system under study. This method follows the steps outlined by Kraus *et al.* [13].

2.1.1. Ground state search

We start by considering a fermionic system in a lattice governed by a Hamiltonian of the form

$$\hat{H} = i \sum_{j,k} T_{jk} \hat{c}_j \hat{c}_k + \sum_{j,k,l,m} U_{jklm} \hat{c}_j \hat{c}_k \hat{c}_l \hat{c}_m, \quad (2.1.1)$$

where each \hat{c}_i is a Majorana operator, T is a matrix satisfying $T = -T^T$, and U is a tensor antisymmetric under the exchange of two adjacent indices. We can identify two distinct terms: a quadratic term,

$$\hat{H}_q = i \sum_{j,k} T_{jk} \hat{c}_j \hat{c}_k, \quad (2.1.2)$$

and an interaction or quartic term,

$$\hat{H}_I = \sum_{j,k,l,m} U_{jklm} \hat{c}_j \hat{c}_k \hat{c}_l \hat{c}_m. \quad (2.1.3)$$

It is easy to notice that the Hubbard Hamiltonian constitutes a particular case of the Hamiltonian in Eq. (2.1.1).

In principle, the fermionic Gaussian state approximation to the ground state could be found via a direct minimization of the energy,

$$\min_{\rho \text{ Gaussian}} \text{Tr}(\rho \hat{H}) = \min_{i \in \hat{\mathbb{I}}} \left\{ \sum_{i,j} T_{ij} \Gamma_{ij} - 3 \sum_{i,j,k,l} U_{ijkl} \Gamma_{ij} \Gamma_{kl} \right\}, \quad (2.1.4)$$

where we have used the expression of the covariance matrix from Eq. (1.2.15) and that Wick's theorem allows us to write

$$\langle \hat{c}_i \hat{c}_j \hat{c}_k \hat{c}_l \rangle = -(\Gamma_{ij} \Gamma_{kl} - \Gamma_{ik} \Gamma_{jl} + \Gamma_{il} \Gamma_{jk}). \quad (2.1.5)$$

Generally, solving that problem is analytically non-trivial and numerically demanding. Therefore, we employ a distinct strategy: we aim to find the ground state via an imaginary time evolution. Every Gaussian state remains Gaussian through a time evolution under a quadratic Hamiltonian. However, due to the presence of the interacting term \hat{H}_I , the time evolution will drive the state out of the set of Gaussian states. In order to avoid that, two approaches can be considered:

1. Evolve the state under the full Hamiltonian for a short amount of time Δt and then projecting the resulting state $\rho(t + \Delta t)$ back to the set of Gaussian states.
2. It can be shown that the real time evolution of the covariance matrix can be viewed as an evolution under a quadratic but state-dependent Hamiltonian of the form

$$\hat{H}_Q = i \sum_{j,k} \bar{h}(\Gamma(t))_{jk} \hat{c}_j \hat{c}_k, \quad (2.1.6)$$

where $\bar{h}(\Gamma(t))$ is defined as

$$\bar{h}(\Gamma(t)) := T + 6 \text{Tr}_B[U\Gamma(t)], \quad (2.1.7)$$

with $\text{Tr}_B(U\Gamma)_{ij} := \sum_{kl} U_{ijkl} \Gamma_{lk}$ [13]. Then, we can perform the imaginary time evolution of the state under such a quadratic but state-dependent Hamiltonian. Since the considered Hamiltonian is indeed quadratic, the Gaussian state remains Gaussian throughout the entire evolution, eliminating the need for projection at each time step. However, the Hamiltonian now depends on the evolving state, requiring it to be updated according to the new state at every time step of the process.

For obtaining the imaginary time evolution equations, we start by considering the imaginary time evolved Gaussian state

$$\rho(\tau) = \frac{e^{-\hat{H}\tau} \rho(0) e^{-\hat{H}\tau}}{\text{Tr} \left[e^{-2\hat{H}\tau} \rho(0) \right]}, \quad (2.1.8)$$

which leads to the following time evolution equation:

$$\frac{d}{d\tau}\rho(\tau) = -\{\hat{H}, \rho(\tau)\} + 2\rho(\tau) \text{Tr}[\hat{H}\rho(\tau)]. \quad (2.1.9)$$

Following the time evolution equation of the density operator, we can find the one from the covariance matrix to be

$$\begin{aligned} \frac{d}{d\tau}\Gamma_{jk}(\tau) &= \frac{i}{2} \frac{d}{d\tau} \text{Tr}[\rho(\tau)[\hat{c}_j, \hat{c}_k]] \\ &= -i \text{Tr}[\{\hat{H}, \hat{c}_j \hat{c}_k\} \rho(\tau)] + 2\Gamma_{jk} \text{Tr}[\hat{H}\rho(\tau)] \end{aligned} \quad (2.1.10)$$

Now, regardless of whether we consider the Hamiltonian to be the quadratic but state-dependent Hamiltonian \hat{H}_Q or we follow the approach where we consider the interacting Hamiltonian and project the state back to the set of Gaussian states for each small time step, the evolution equation of the covariance matrix can be found to be described by

$$\begin{aligned} \frac{d}{d\tau}\Gamma(\tau) &= -4(\Gamma\bar{h}(\Gamma)\Gamma + \bar{h}(\Gamma)) \\ &= [A(\Gamma), \Gamma], \end{aligned} \quad (2.1.11)$$

where we have used that for a pure Gaussian state $\Gamma^2 = -\mathbb{1}$ and defined

$$A(\Gamma) := 2[\bar{h}(\Gamma), \Gamma]. \quad (2.1.12)$$

It is interesting to note that any pure state remains pure under an evolution through Eq. (2.1.11) since

$$\frac{d}{d\tau}\Gamma^2 = \Gamma \frac{d\Gamma}{d\tau} + \frac{d\Gamma}{d\tau} \Gamma = -4(\Gamma^2\bar{h}(\Gamma)\Gamma + \Gamma\bar{h}(\Gamma) + \Gamma\bar{h}(\Gamma)\Gamma^2 + \bar{h}(\Gamma)) = 0, \quad (2.1.13)$$

where we used that all pure Gaussian states fulfill $\Gamma^2 = -\mathbb{1}$. Furthermore, we can also observe that the energy of the state always decreases under such an evolution:

$$\begin{aligned} \frac{d}{d\tau}E(\tau) &= \sum_{jk} \frac{\partial E}{\partial \Gamma_{jk}} \frac{d}{d\tau}\Gamma_{jk} = \sum_{jk} \bar{h}(\Gamma)_{jk} \frac{d}{d\tau}\Gamma_{jk} \\ &= 4 \text{Tr}[\bar{h}(\Gamma\bar{h}(\Gamma)\Gamma + \bar{h}(\Gamma))] = 2 \text{Tr}[[\bar{h}, \Gamma]^2] \leq 0, \end{aligned} \quad (2.1.14)$$

where we have used that $[\bar{h}, \Gamma]$ is antisymmetric and, therefore, $[\bar{h}, \Gamma]^2$ is negative-definite. This energy evolution is interesting because it implies that the state reaches a stationary point iff $[\bar{h}, \Gamma] = 0$, which suggests us a possible convergence criterion for the imaginary time evolution.

To conclude, if we start from a pure state, Eq. (2.1.11) can be formally integrated. Its solution is given by

$$\Gamma(t) = O(t)\Gamma(0)O(t)^T \quad (2.1.15)$$

with

$$O(t) = \mathcal{T} \exp\left(\int_0^t A(\Gamma(\tau'))d\tau'\right), \quad (2.1.16)$$

where \mathcal{T} is the time-ordering operator.

2.2. MPS conversion of Gaussian states

The ultimate goal is to use our Gaussian state approximation of the ground state as the initial state for the DMRG algorithm. To achieve this, it is essential to obtain its representation in MPS form. We start by recalling that in the Dirac representation, the covariance matrix of a Gaussian state is given by

$$\Gamma^{\text{dir}} = \begin{pmatrix} \langle \hat{a}_j^\dagger \hat{a}_i \rangle & \langle \hat{a}_j \hat{a}_i \rangle \\ \langle \hat{a}_j^\dagger \hat{a}_i^\dagger \rangle & \langle \hat{a}_j \hat{a}_i^\dagger \rangle \end{pmatrix}_{1 \leq i, j \leq n}. \quad (2.2.1)$$

Since our state is pure, it will be the ground state of a quadratic Hamiltonian. Our strategy will then consist on finding the ground state MPS of our Gaussian state's parent Hamiltonian.

2.2.1. Covariance matrix with vanishing off-diagonal terms

We start by evaluating the case in which the pairing terms of the covariance matrix are absent, i.e., $\langle \hat{a}_j \hat{a}_i \rangle = \langle \hat{a}_j^\dagger \hat{a}_i^\dagger \rangle = 0 \forall i, j$. The parent Hamiltonian will be of the form

$$\hat{H} = \sum_{i, j=1}^n t_{ij} \hat{a}_i^\dagger \hat{a}_j, \quad (2.2.2)$$

where n is the number of fermionic modes. The Hamiltonian corresponds to the free fermions case and its diagonalization through a unitary transformation U leads to

$$\hat{H} = \sum_{i, j, k, l=1}^n \hat{a}_i^\dagger U_{ik} \epsilon_k \delta_{kl} U_{lj}^\dagger \hat{a}_j = \sum_{k=1}^n \epsilon_k \hat{d}_k^\dagger \hat{d}_k, \quad (2.2.3)$$

where we have defined the eigenmodes $\hat{d}_k := \sum_{j=1}^n U_{kj}^\dagger \hat{a}_j$. Now, let's assume that the first m eigenmodes have negative eigenenergy, i.e., $\epsilon_k < 0$ for $1 \leq k \leq m$. Then, the ground state is given simply by

$$|GS\rangle = \prod_{k=1}^m \hat{d}_k^\dagger |0\rangle. \quad (2.2.4)$$

Since we have access to the covariance matrix of the ground state and the same unitary transformation that diagonalizes the Hamiltonian is the one that diagonalizes the covariance matrix, we can obtain the occupied eigenmodes simply by diagonalizing its upper-left block,

$$\gamma_{ij} := \langle \hat{a}_j^\dagger \hat{a}_i \rangle = \sum_{k=1}^n U_{ik} n_k U_{kj}^\dagger, \quad (2.2.5)$$

where $n_k = 1$ for $1 \leq k \leq m$ and $n_k = 0$ for $m < k \leq n$.

It follows from Eq. (2.2.4), that in order to build the MPS of the ground state, we need to successively apply the MPOs of each occupied eigenmode to the MPS

of the vacuum state. However, the lowest possible bond dimension for any MPO representing one of the occupied eigenmodes is 2, which means that the final bond dimension of the ground state MPS will be 2^m . As this number is typically large, we will need a truncation scheme to keep a manageable bond dimension $D \ll 2^m$. A popular strategy consists on, after each MPO application:

1. Bring the MPS into right-canonical form.
2. Perform an SVD decomposition on the orthogonality center $C_l = USV^\dagger$ while only keeping the D largest singular values.
3. Shift the orthogonality center, i.e., $C_l \rightarrow A_l = U$ and $B_{l+1} \rightarrow C_{l+1} = SV^\dagger B_{l+1}$, where A and B are left and right isometries, respectively.
4. Repeat steps 2 and 3 until reaching the last site.
5. When the orthogonality center reaches the last site, perform an additional SVD $C_N = USV^\dagger$ and just update $C_N \rightarrow A_N = U$. That ensures that the state after the truncation is normalized and in left-canonical form.

As a result of truncating the bond dimension, an error on the MPS representation is introduced. In order to reduce such truncation error, it is highly advisable to express the eigenmodes through Wannier orbitals. This operators are more localized in space as they correspond to the eigenstates of the position operator projected onto the space of occupied modes [27]. The position operator is given by $\hat{X} = \sum_{k=1}^n k \hat{a}_k^\dagger \hat{a}_k$ and its projection in the eigenmode basis is simply

$$X_{ij} = \langle 0 | \hat{d}_i^\dagger \hat{X} \hat{d}_j^\dagger | 0 \rangle = \sum_{k=1}^n k U_{ik}^\dagger U_{kj}. \quad (2.2.6)$$

Being V the unitary matrix that diagonalizes the position operator, we can now define the Wannier orbitals as

$$\hat{f}_l = \sum_{k=1}^m V_{lk}^\dagger \hat{d}_k = \sum_{k=1}^m \sum_{j=1}^n V_{lk}^\dagger U_{kj}^\dagger \hat{a}_j. \quad (2.2.7)$$

Now, it can be shown that the ground state in terms of the Wannier orbitals is just

$$|GS\rangle = \prod_{k=1}^m \hat{d}_k^\dagger |0\rangle = \prod_{k=1}^m \hat{f}_k^\dagger |0\rangle. \quad (2.2.8)$$

In order to find the MPO representation of the Wannier orbitals we have to take into account that in the spin-1/2 there are 2 possible fermionic modes per site. If we do the transformation $\hat{a}_{2j-1(2j)}^\dagger \rightarrow \hat{a}_{j,\uparrow(j,\downarrow)}^\dagger$, the Wannier orbitals can be written as

$$\hat{f}_k^\dagger = \sum_{j=1}^N \left([UV]_{2j-1,k} \hat{a}_{j,\uparrow}^\dagger + [UV]_{2j,k} \hat{a}_{j,\downarrow}^\dagger \right), \quad (2.2.9)$$

where N is the total number of sites. Then, the MPO representing each Wannier

orbital will simply be

$$\hat{f}_k^\dagger = (\hat{0} \quad \hat{1}) \prod_{l=1}^N W_l^{[k]} \begin{pmatrix} \hat{1} \\ \hat{0} \end{pmatrix}, \quad (2.2.10)$$

with

$$W_l^{[k]} = \begin{pmatrix} \hat{1}_l & \hat{0}_l \\ [UV]_{2l-1,k} \hat{a}_{l,\uparrow}^\dagger + [UV]_{2l,k} \hat{a}_{l,\downarrow}^\dagger & \hat{Z}_l \end{pmatrix}, \quad (2.2.11)$$

and

$$\hat{Z}_l = \begin{pmatrix} 1 & 0 & 0 & 0 \\ 0 & -1 & 0 & 0 \\ 0 & 0 & -1 & 0 \\ 0 & 0 & 0 & 1 \end{pmatrix}_l \quad (2.2.12)$$

being the parity operator acting on site l .

To conclude, we simply need to apply the MPOs of the Wannier orbitals successively. In practice, it has been observed that to minimize truncation errors further, it is more effective to apply them in a "left-meet-right" order [28]. This approach involves alternately applying the operators localized at the edges and gradually moving toward the center (Fig. 2.1).

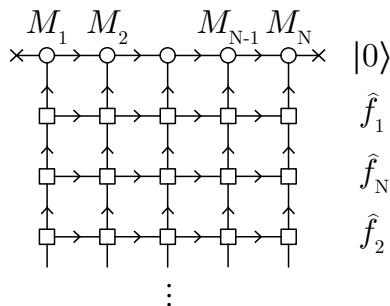


Figure 2.1.: Graphic representation of the method to obtain the Fermi sea ground state via the successive application of the MPOs representing Wannier orbitals to the MPS of the vacuum state. The MPOs are applied in the "left-meet-right" order.

2.2.2. General case

In the general case, the parent Hamiltonian corresponds to the one introduced in Eq. (1.2.20). As stated in Sec. 1.2.5, the ground state of such Hamiltonian is the vacuum of its eigenmodes, which receives the name of Bogoliubov vacuum. Our goal is then to find an efficient MPS representation of such state. We will follow the method described in Jin *et al.* [29].

Consider that we have N fermionic modes and we divide the system in two subsystems A and B . Being A the subsystem composed by M fermionic modes $i = 1, 2, \dots, M$, the covariance matrix of its reduced density operator will take the form

$$\Gamma_A^{\text{dir}} = \begin{pmatrix} \langle \hat{a}_j^\dagger \hat{a}_i \rangle & \langle \hat{a}_j \hat{a}_i \rangle \\ \langle \hat{a}_j^\dagger \hat{a}_i^\dagger \rangle & \langle \hat{a}_j \hat{a}_i^\dagger \rangle \end{pmatrix}_{1 \leq i, j \leq M}. \quad (2.2.13)$$

The Bogoliubov transformation of the reduced subsystem diagonalizes the Hamil-

tonian and is given by

$$B_A = \begin{pmatrix} U_A & V_A^* \\ V_A & U_A^* \end{pmatrix} \quad (2.2.14)$$

where U_A and V_A are matrices satisfying the relations $U_A^\dagger U_A + V_A^\dagger V_A = \mathbb{1}$ and $U_A^\dagger V_A^* + V_A^\dagger U_A^* = 0$. Those relations are a direct consequence of the unitarity of B_A . The Bogoliubov transformation defines the eigenmodes of the system as

$$\hat{d}_{A,k} = \sum_{j=1}^M \left(\hat{a}_j^\dagger [V_A]_{jk}^* + \hat{a}_j [U_A]_{jk}^* \right), \quad (2.2.15)$$

which bring the covariance matrix into diagonal form,

$$\Gamma_A^{\text{dir}} = B_A \begin{pmatrix} \Lambda_A & 0 \\ 0 & \mathbb{1} - \Lambda_A \end{pmatrix} B_A^\dagger, \quad (2.2.16)$$

where $[\Lambda_A]_{ij} = \lambda_i \delta_{ij}$ and $\lambda_i \in [0, 1] \forall i$. The eigenvalues i -th and $(M+i)$ -th are then paired and their corresponding eigenvectors are the i -th and $(M+i)$ -th columns of the Bogoliubov transformation. An interchange of those columns in the Bogoliubov matrix correspond to a particle-hole transformation $\hat{d}_{A,i}^\dagger \leftrightarrow \hat{d}_{A,i}$.

It can be seen from the diagonalized covariance matrix that the eigenmodes allow to express the density operator as

$$\hat{\rho}_A = \prod_{k=1}^M \left[\lambda_k \hat{d}_{A,k}^\dagger \hat{d}_{A,k} + (1 - \lambda_k) \hat{d}_{A,k} \hat{d}_{A,k}^\dagger \right]. \quad (2.2.17)$$

The eigenstates of the density operator are the Fock states of d_A modes,

$$|m_A\rangle = (\hat{d}_{A,1}^\dagger)^{m_1} \dots (\hat{d}_{A,M}^\dagger)^{m_M} |0\rangle_{d_A}, \quad (2.2.18)$$

where $|0\rangle_{d_A}$ is the vacuum of d_A modes, $m_i \in 0, 1$ is the occupation number of the i -th eigenmode and $m_A = m_1, m_2, \dots, m_M$ labels each Fock state. These Fock states can also be expressed in terms of the Fock states of the subsystem $A-1$, defined as the subsystem A with the M -th mode excluded and the local space of the M -th mode,

$$|m_A\rangle = \sum_{m_{A-1}} \sum_{n_M=0,1} [C_A]_{m_A}^{m_{A-1}, n_M} |m_{A-1}\rangle |n_M\rangle, \quad (2.2.19)$$

where $|n_M\rangle = (\hat{a}^\dagger)^{n_M} |0\rangle$ and

$$[C_A]_{m_A}^{m_{A-1}, n_M} = (\langle n_M | \otimes \langle m_{A-1} |) |m_A\rangle. \quad (2.2.20)$$

Therefore, by starting with a subsystem of only one fermionic mode and iteratively increasing its size one by one, we can get an MPS expression for our ground state

$$\begin{aligned} |GS\rangle &= |0\rangle_{d_N} \\ &= \sum_{\vec{m}, \vec{n}} [C_A]_{m_1}^{n_1} [C_A]_{m_2}^{m_1, n_2} \dots [C_A]_{m_{A-1}}^{m_{A-2}, n_{A-1}} [C_A]_0^{m_{A-1}, n_A} |n_1\rangle |n_2\rangle \dots |n_{N-1}\rangle |n_N\rangle, \end{aligned} \quad (2.2.21)$$

where $\vec{m}[\vec{n}] = (m_1, \dots, m_{N-1})[(n_1, \dots, n_N)]$. Hence, the problem has been reduced to the computation of certain overlaps. It is interesting to highlight that, thanks to the possibility of performing a particle-hole transformation by interchanging the proper columns of the Bogoliubov transformation, any Fock state can be expressed as the vacuum of the appropriate Bogoliubov transformation. Consequently, it is enough to explain how to calculate the overlaps between Bogoliubov vacua, i.e., of the form $(\langle n_M | \otimes \langle 0 |_{d_{A-1}}) | 0 \rangle_{d_A}$.

Before explaining how to calculate those overlaps, we can notice that the bond dimension of our MPS scales exponentially with the size of the system. In order to avoid that, a truncation protocol is required. We introduce two possible schemes:

- *Gaussian truncation.* It consists on setting a small truncation value ϵ such that if $\lambda_i < \epsilon$ ($\lambda_i > 1 - \epsilon$) for some i , we will only consider the Fock states in which that i mode is empty (occupied), reducing by a factor of 2 the bond dimension per every value λ_i that satisfies one of this two conditions. This truncation protocol preserves the Gaussian nature of the state.
- *SVD truncation.* We compute the density operator eigenvalues for each Fock state and only keep the Fock states associated with the largest ones. This protocol is more precise than Gaussian truncation, but it can be more computationally expensive.

For the results shown in Chapter 3, we used a mixed approach. We did a preselection of D' Fock states by using the Gaussian truncation. Afterward, we computed its associated density operator eigenvalues and keep those with the $D < D'$ largest ones.

Now we can start to explain how to properly compute overlaps of the shape of Eq. (2.2.20), where the main difficulty arises from the fact that $|m_{A-1}\rangle$ and $|m_A\rangle$ are built over two different Bogoliubov vacua. We start by introducing the Bloch-Messiah decomposition [30], which allows to write the matrices U_A and V_A from the Bogoliubov transformation as $U_A = D_A \bar{U}_A C_A$ and $V_A = D_A^* \bar{V}_A C_A$, where D_A and C_A are unitary matrices and \bar{U}_A and \bar{V}_A are of the form

$$\bar{U}_A = \begin{pmatrix} \mathbb{1} & & \\ & \oplus_k u_p \sigma^0 & \\ & & 0 \end{pmatrix}, \quad \bar{V}_A = \begin{pmatrix} 0 & & \\ & \oplus_k i v_p \sigma^y & \\ & & \mathbb{1} \end{pmatrix} \quad (2.2.22)$$

with u_p and v_p satisfying $u_p^2 + v_p^2 = 1$ and $u_p, v_p \geq 0$, and σ^0 and σ^y being the 2×2 identity and Pauli-Y matrix, respectively. A detailed explanation on how to numerically perform this decomposition can be found in Appendix A.

After performing the Bloch-Messiah decomposition, the Bogoliubov transformation can be expressed as

$$B = \begin{pmatrix} D_A & 0 \\ 0 & D_A^* \end{pmatrix} \begin{pmatrix} \bar{U}_A & \bar{V}_A \\ \bar{V}_A & \bar{U}_A \end{pmatrix} \begin{pmatrix} C_A & 0 \\ 0 & C_A^* \end{pmatrix}, \quad (2.2.23)$$

which allow the d_A modes to be seen as the result of three successive canonical

transformations

$$(\hat{d}_A^\dagger \quad \hat{d}_A) = (\hat{a}^\dagger \quad \hat{a}) \begin{pmatrix} D_A & 0 \\ 0 & D_A^* \end{pmatrix} \begin{pmatrix} \bar{U}_A & \bar{V}_A \\ \bar{V}_A & \bar{U}_A \end{pmatrix} \begin{pmatrix} C_A & 0 \\ 0 & C_A^* \end{pmatrix}, \quad (2.2.24)$$

where the operators without indices represent row vectors, e.g., $\hat{a}^\dagger = (\hat{a}_1^\dagger, \dots, \hat{a}_M^\dagger)$. To help us understand the structure of the Bogoliubov vacua, we can define the b modes as $\hat{b}^\dagger = \hat{a}^\dagger D_A$. Then, we can see that the identity block $\mathbb{1}$ (null block 0) in \bar{V}_A corresponds to fully occupied (empty) b modes in the vacuum $|0\rangle_{d_A}$. As a and b modes share the same vacuum, we can rewrite the Bogoliubov vacuum as [31]

$$|0\rangle_{d_A} = \prod_{k \in O} \hat{b}_k^\dagger \prod_{p \in P} (u_p + v_p \hat{b}_p^\dagger \hat{b}_{-p}^\dagger) |0\rangle_a \quad (2.2.25)$$

where O (P) denotes the set of fully occupied (paired) b modes. We can now define f modes as $\hat{f} = \hat{b}^\dagger \bar{V}_A + \hat{b} \bar{U}_A = \hat{a}^\dagger D_A \bar{V}_A + \hat{a} D_A^* \bar{U}_A$ and rewrite Eq. (2.2.25) as

$$|0\rangle_{d_A} = \frac{1}{\prod_{p \in P} v_p} \prod_{k \in O} \hat{f}_k \prod_{p \in P} \hat{f}_p \hat{f}_{-p} |0\rangle_a. \quad (2.2.26)$$

We can find an analogous expression for $|0\rangle_{d_{A-1}}$ which allows us to write

$$|0\rangle_{d_{A-1}} |n_M\rangle = \frac{1}{\prod_{p \in P'} v'_p} \prod_{k \in O'} \hat{f}'_k \prod_{p \in P'} \hat{f}'_p \hat{f}'_{-p} (f'_M)^{n_M} |0\rangle_a, \quad (2.2.27)$$

where we have defined $\hat{f}'_M := \hat{a}_M^\dagger$ and, in general, $\hat{f}' = \hat{a}^\dagger D'_A \bar{V}'_A + \hat{a} D_A'^* \bar{U}'_A$ with

$$D'_A = D_{A-1} \oplus 1, \quad \bar{U}'_A = \bar{U}_{A-1} \oplus (1 - n_m), \quad \bar{V}'_A = \bar{V}_{A-1} \oplus n_m. \quad (2.2.28)$$

Finally, we can compute the overlap as

$$\langle n_M | \otimes \langle 0 |_{d_{A-1}} |0\rangle_{d_A} = (-1)^{\bar{M}(\bar{M}-1)/2} \text{Pf} \begin{pmatrix} \bar{V}_A'^T \bar{U}'_A & \bar{V}_A'^T D_A'^\dagger D_A \bar{V}_A \\ -\bar{V}_A'^T D_A'^T D_A^* \bar{V}'_A & \bar{U}_A'^T \bar{V}_A \end{pmatrix}, \quad (2.2.29)$$

where \bar{M} correspond to the number of f' modes and the matrices within the Pfaffian only contain the rows and columns corresponding to the fully occupied and paired f modes [32].

2.3. Description of the algorithm

In this section, a detailed description of the algorithm used to obtain the MPS representation of the initial Gaussian state is provided.

The main steps of the algorithm are:

1. Find matrices T and U such that the Hamiltonian in Eq. (2.1.1) corresponds to the Hubbard Hamiltonian with our desired values for the hopping t , interaction U and chemical potential μ terms.
2. Obtain the covariance matrix representing the ground state of the quadratic

term of our Hamiltonian. This is done by following the procedure described in Sec. 1.2.5.

The obtained covariance matrix will be used as the initial state for the imaginary time evolution. Since the evolution takes place under the action of an effective quadratic Hamiltonian, the only quantum number that will be preserved is the parity. Therefore, it is vital that our initial Gaussian state lies in the same symmetry sector as the final ground state. If we are performing a calculation for $\mu = 0$, the ground state will correspond to the half-filling setting and, therefore, the parity corresponds to that of the number of sites. However, for $\mu \neq 0$ it is typically non-trivial to know before-hand the parity of the final state. In that case, it is advised to generate both an even and an odd covariance matrix and check which of the converged states has a lower energy.

The parity of the fermionic Gaussian state with covariance matrix Γ can be obtained through the Wick's theorem as $P = \text{Pf}(\Gamma)$. One can obtain a covariance matrix representing a state with the opposite parity by defining a matrix $U := \text{diag}(1, 1, \dots, 1, -1)$ and computing $\tilde{\Gamma} = U\Gamma U^\dagger$.

3. Perform the imaginary time evolution with

$$\Gamma(\tau + \Delta\tau) = O(\Delta\tau)\Gamma(\tau)O(\Delta\tau)^T, \quad O(\Delta\tau) = \exp(A(\Gamma(\tau))\Delta\tau). \quad (2.3.1)$$

In our case, we have used time steps whose length decays logarithmically to accelerate the initial part of the time evolution. As our convergence criteria, we choose a small value ϵ_{it} and assume that the evolution has converged when two conditions are met:

- The energy difference between the two last time steps ΔE satisfies $\Delta E < \epsilon_{it}$.
- The Frobenius norm of the matrix $[\bar{h}, \Gamma]$ satisfies $\|[\bar{h}, \Gamma]\|_F < \epsilon_{it}$, where Γ is the covariance matrix and \bar{h} is the matrix defined in Eq. (2.1.7).

4. Transform the converged covariance matrix into its Dirac representation.
5. Compute the Frobenius norm of one of its off-diagonal blocks, e.g., $\|\langle \vec{a}\vec{a}^T \rangle\|_F$ with $\vec{a} = (\hat{a}_1, \hat{a}_2, \dots, \hat{a}_N)^T$.
6. Set a small parameter ϵ_{MPS} . If $\|\langle \vec{a}\vec{a}^T \rangle\|_F < \epsilon_{MPS}$, we compress the Gaussian state into an MPS using the Fermi sea approach described in Sec. 2.2.1. Otherwise, we follow the Pfaffian method introduced in Sec. 2.2.2.
7. Due to the accumulation of numerical errors, the covariance matrix in the Dirac representation can have some coefficients with non-vanishing imaginary terms. In that case, the final MPS will also have complex entries, which can significantly increase the computation time of the DMRG calculation. In order to avoid that we realize that, since the Hamiltonian is Hermitian, given a ground state $|\psi_0\rangle$ with complex entries, we can define another state $|\psi'_0\rangle := 1/\sqrt{2}(|\psi_0\rangle + |\psi_0^*\rangle)$ such that it has the same energy. In terms of MPS, each tensor M'_l of $|\psi'_0\rangle$ will be

$$M'_l = \frac{1}{\sqrt{2}}(M_l \oplus M_l^*) = \frac{1}{\sqrt{2}} \begin{pmatrix} M_l & 0 \\ 0 & M_l^* \end{pmatrix} \quad (2.3.2)$$

with M_l being the site l tensor of the MPS representation of $|\psi_0\rangle$ and the matrix indices being the bond indices χ_{l-1} and χ_l . If we split each tensor M_l into its real M_l^R and imaginary M_l^I parts, we can write

$$M_l = \frac{1}{\sqrt{2}} \begin{pmatrix} M_l^R + iM_l^I & 0 \\ 0 & M_l^R - iM_l^I \end{pmatrix} = \frac{1}{\sqrt{2}} (\mathbb{1} \otimes M_l^R + i\sigma^Z \otimes M_l^I) \quad (2.3.3)$$

with σ^Z being the Pauli- Z matrix.

Finally, we can apply a $\pi/2$ -rotation around the X - axis,

$$\begin{aligned} M_l' &= \frac{1}{\sqrt{2}} (\mathbb{1} \otimes M_l^R + ie^{-i\frac{\pi}{4}\sigma^X} \sigma^Z e^{i\frac{\pi}{4}\sigma^X} \otimes M_l^I) = \frac{1}{\sqrt{2}} (\mathbb{1} \otimes M_l^R - i\sigma^Y \otimes M_l^I) \\ &= \begin{pmatrix} M_l^R & -M_l^I \\ M_l^I & M_l^R \end{pmatrix}, \end{aligned} \quad (2.3.4)$$

such that all the entries of M_l' are real.

8. Initialize the DMRG calculation with the computed MPS as the initial state. In our case, we have used both two-site and CBE DMRG for obtaining the results of Chapter 3.
9. Compute and store the energy, the local density distribution and the local spin distribution of the state after each sweep has been completed. That is done to have a better understanding on the ground state search process.
10. Continue the DMRG calculation until one of the two following events takes place: a maximum number of sweeps previously set is reached, or a convergence criterion is met.

In our implementation, we allow to choose between a fixed or an adaptive maximum bond dimension. If the maximum bond dimension is fixed, the convergence criterion consists on setting a value ϵ_1 such that if the energy difference between the last two sweeps ΔE is smaller than that value, DMRG stops. If the maximum bond dimension is allowed to increase, the algorithm does not stop when $\Delta E < \epsilon_1$. Instead, it increases the maximum allowed bond dimension. For this scenario, we introduce a second threshold value ϵ_2 . If the energy difference between the last sweep at the current maximum bond dimension and the last sweep at the previous maximum bond dimension is smaller than ϵ_2 , the DMRG algorithm stops.

3. Numerical results

In this chapter, we present some benchmarks of the fermionic Gaussian state MPS obtention procedure, showing the accuracy of the imaginary time evolution and its posterior MPS conversion. Additionally, we compare the DMRG ground state search performance when initialized with either a product or a Gaussian state. The DMRG algorithms used for the comparison are two-site and CBE DMRG. We examine two scenarios: one where the ground state is at half-filling and another corresponding to the 1/8-hole-doped configuration.

3.1. Benchmarks for the initial fermionic Gaussian state MPS obtention

We started by conducting some benchmarks to guarantee that the method employed to obtain the fermionic Gaussian state MPS used to initialize DMRG works appropriately.

First, we compared the imaginary time evolution result to the one obtained via direct minimization of Eq. (2.1.4). It is shown in Ref. [26] that for the attractive Hubbard model in a lattice of size $n \times n$ and with periodic boundary conditions, the best variational energy of a fermionic Gaussian state is given by

$$E(\mu) = \min_{d^2 \leq \eta} \left\{ -\text{Tr} \left[\sqrt{h_0^2 + 2Udh_0 + U^2\eta} \right] - U\eta n^2 \right\} - \mu n^2, \quad (3.1.1)$$

where d and η are the optimization parameters, U and μ are the interaction and chemical potential terms, respectively, of the Hubbard Hamiltonian as introduced in Eq. (1.1.4), and h_0 is a matrix such that the quadratic part of the Hubbard Hamiltonian can be written as

$$\hat{H}_q = -t \sum_{\langle i,j \rangle, \sigma} \left(\hat{a}_{i,\sigma}^\dagger \hat{a}_{j,\sigma} + \hat{a}_{j,\sigma}^\dagger \hat{a}_{i,\sigma} \right) - \mu \sum_{i,\sigma} \hat{n}_{i,\sigma} = \sum_{\sigma} \vec{a}_{\sigma}^\dagger h_0 \vec{a}_{\sigma} \quad (3.1.2)$$

with $\vec{a}_{\sigma} = (\hat{a}_{1,\sigma}, \hat{a}_{2,\sigma}, \dots, \hat{a}_{N-1,\sigma}, \hat{a}_{N,\sigma})^T$.

We considered an 8×8 lattice with periodic boundary conditions. The hopping term t was set as the energy scale, i.e., $t = 1$, and we evaluated the half-filling case for different values of the interaction term (Fig. 3.1). We observe that the imaginary time evolution rapidly converges to the expected ground state. We have also examined the case away from half-filling for different chemical potential values and a fixed attractive interaction $U = -5$ (Fig. 3.2). The results have also shown excellent convergence.

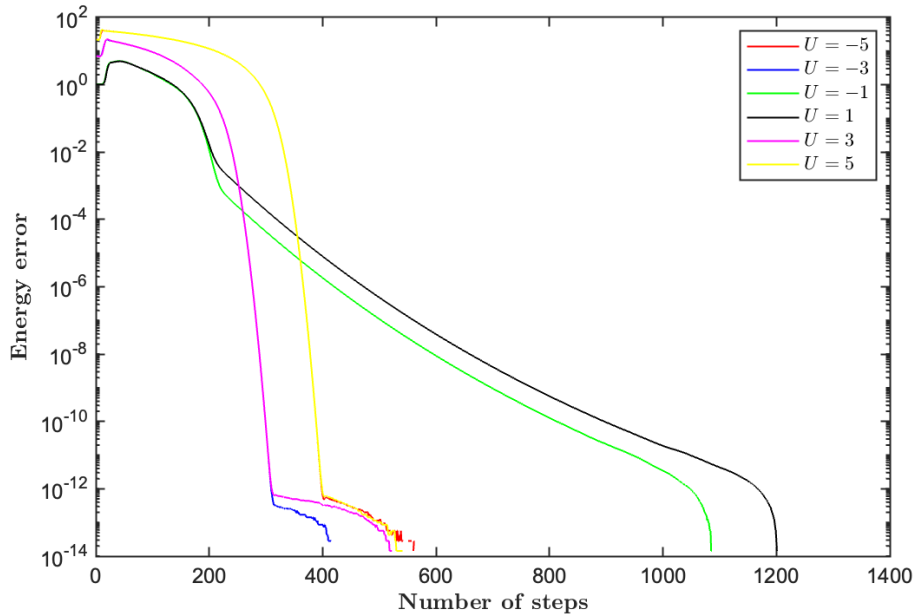


Figure 3.1.: Evolution of the difference between the imaginary time evolution energy and the analytical ground state energy found via direct minimization of Eq. (3.1.1). The calculations correspond to the Hubbard model in an 8×8 lattice with periodic boundary conditions and parameters $t = 1$ and $\mu = 0$.

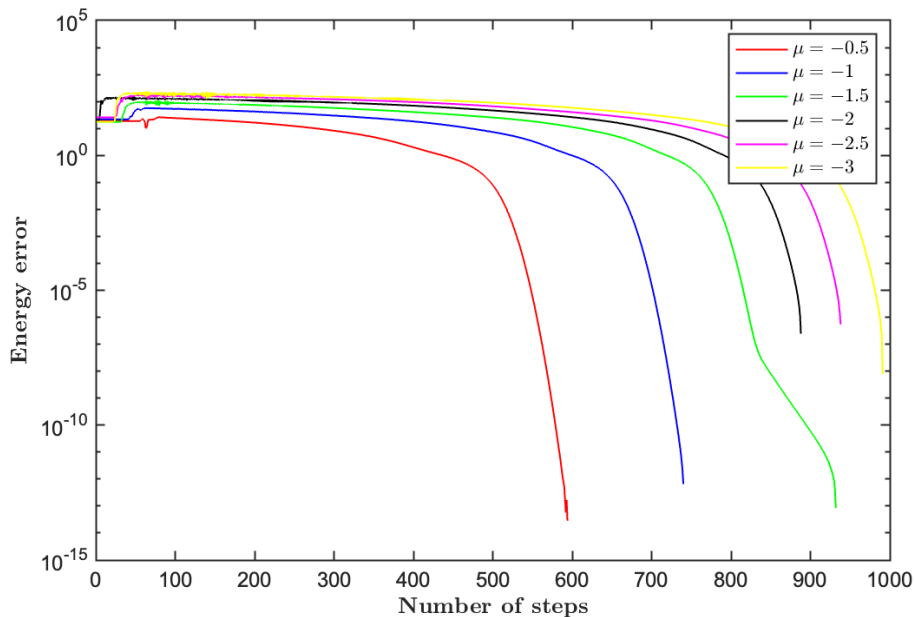


Figure 3.2.: Evolution of the difference between the imaginary time evolution energy and the analytical ground state energy found via direct minimization of Eq. (3.1.1). The calculations correspond to the Hubbard model in an 8×8 lattice with periodic boundary conditions and parameters $t = 1$ and $U = -5$.

To conclude, we have benchmarked the MPS conversion process by checking the

maximum bond dimension dependence of the per-site energy difference between the fermionic Gaussian state and the resulting MPS. The test has been performed in a 4×8 cylinder for both a case where the Fermi sea approach described in Sec. 2.2.1 was suitable and a case where the Pfaffian method introduced in Sec. 2.2.2 was needed (Fig. 3.3). The results show the expected behavior in which the per-site energy difference tends to vanish as the maximum bond dimension D increases, suggesting that the MPS properly represents the fermionic Gaussian state.

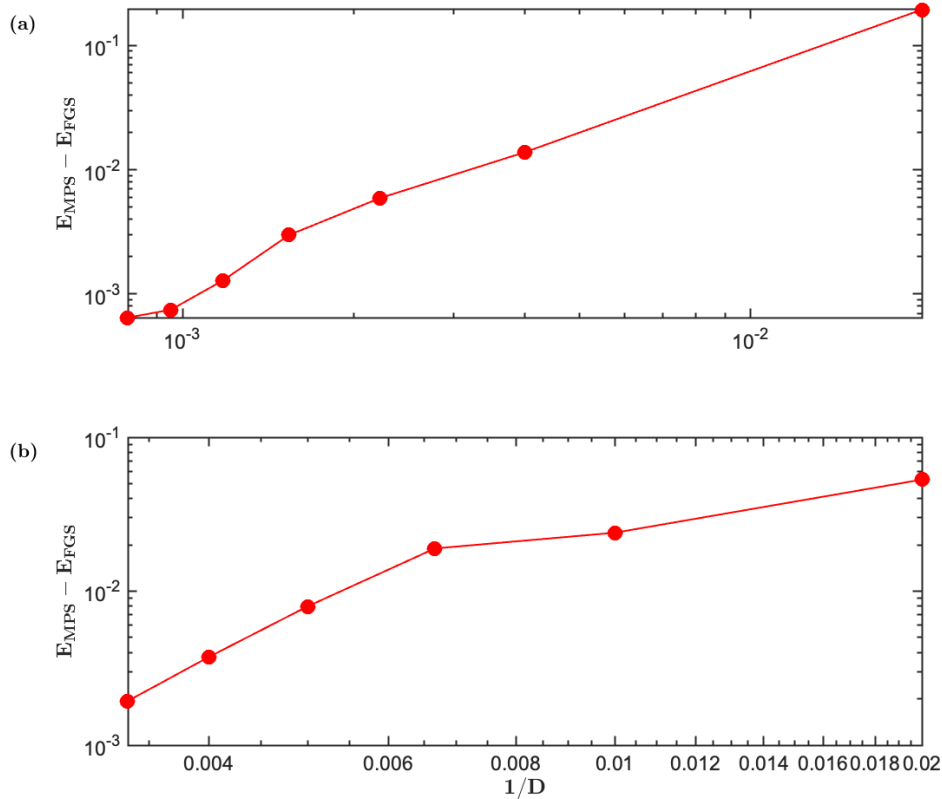


Figure 3.3.: Bond dimension dependence of the per-site energy difference between the fermionic Gaussian state and the MPS representing it. The calculations correspond to a 4×8 cylinder with Hubbard parameters $t = 1$ and $\mu = 0$. The interaction terms are (a) $U = 1$ and (b) $U = -5$. The MPS conversion methods employed have been (a) the Fermi sea approach described in Sec. 2.2.1 and (b) the Pfaffian method described in Sec. 2.2.2.

3.2. Comparison of the DMRG performance

3.2.1. Half-filling case

We began our calculations by considering the simplest case, where the chemical potential μ vanishes. In this scenario, the total particle charge of the ground state equals the number of sites, making it straightforward to determine the quantum numbers that a product state should have so that it is not guaranteed to converge

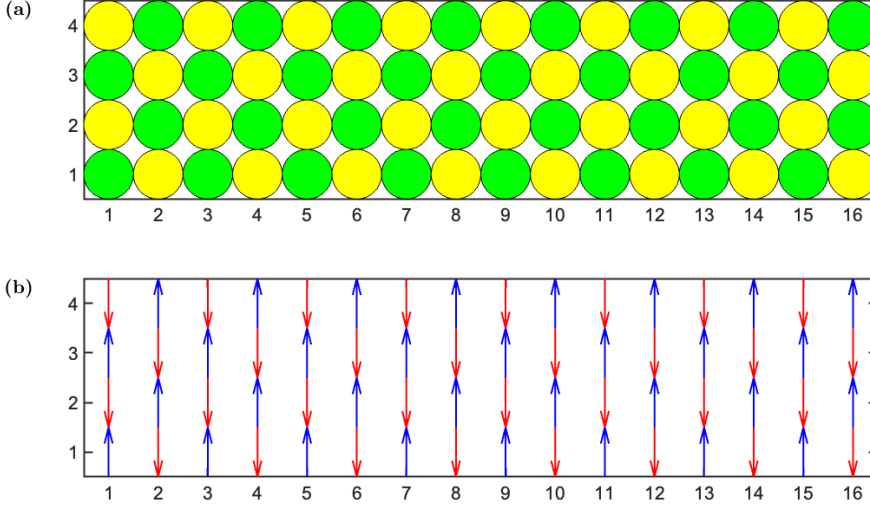


Figure 3.4.: Density and spin distributions of the initial product state for the (a) attractive and (b) repulsive cases in a 4×16 cylinder at half-filling. Yellow circles represent particles, and green circles represent holes relative to the half-filling setting. The size of the circles and arrows is proportional to the magnitude of the corresponding quantities.

to a local minimum. Additionally, for large repulsive interactions, we expect the ground state to exhibit an antiferromagnetic configuration, while for large attractive interactions, we anticipate the formation of singlets consisting of pairs of fermions with opposing spins on a site.

We can employ this knowledge to accelerate the convergence of the product state calculation by initializing the method with a product state composed of pairs of opposing spin fermions for $U < 0$, i.e., $|\uparrow\downarrow, 0, \uparrow\downarrow, 0, \dots\rangle$, and a fully antiferromagnetic product state for $U > 0$, i.e., $|\uparrow, \downarrow, \uparrow, \downarrow, \dots\rangle$ (Fig. 3.4).

Firstly, we ran a DMRG calculation for a relatively low bond dimension $D = 1000$ considering three cylinders of sizes 4×16 , 4×24 , and 8×8 . In each case, we set the hopping term t as our energy scale, i.e., $t = 1$, and fixed an interaction $U = 5$ (Fig. 3.5). We assumed convergence to the ground state when the energy difference between the last sweep and the previous one was lower than a specific value.

We begin by noting that, even with a low maximum bond dimension, the time required to obtain the initial Gaussian state is not particularly significant compared to the DMRG calculation. Moreover, the number of sweeps needed for convergence is lower when initializing DMRG with a Gaussian state. However, in terms of overall time performance, both initial states perform similarly, except in the 8×8 cylinder case, where the Gaussian state requires approximately 40% less time to converge.

In terms of energy, the Gaussian state converged to a lower energy state in every case. The energy differences ΔE between the final states of each cylinder follow the relation: $\Delta E_{4 \times 16} \lesssim \Delta E_{4 \times 24} < \Delta E_{8 \times 8}$. For the 4×16 and the 4×24 cylinders, the energy difference is close to the convergence criteria, indicating that both initial states are approaching similar final states. In contrast, for the 8×8 cylinder, the energy difference between the final states is two orders of magnitude larger than the

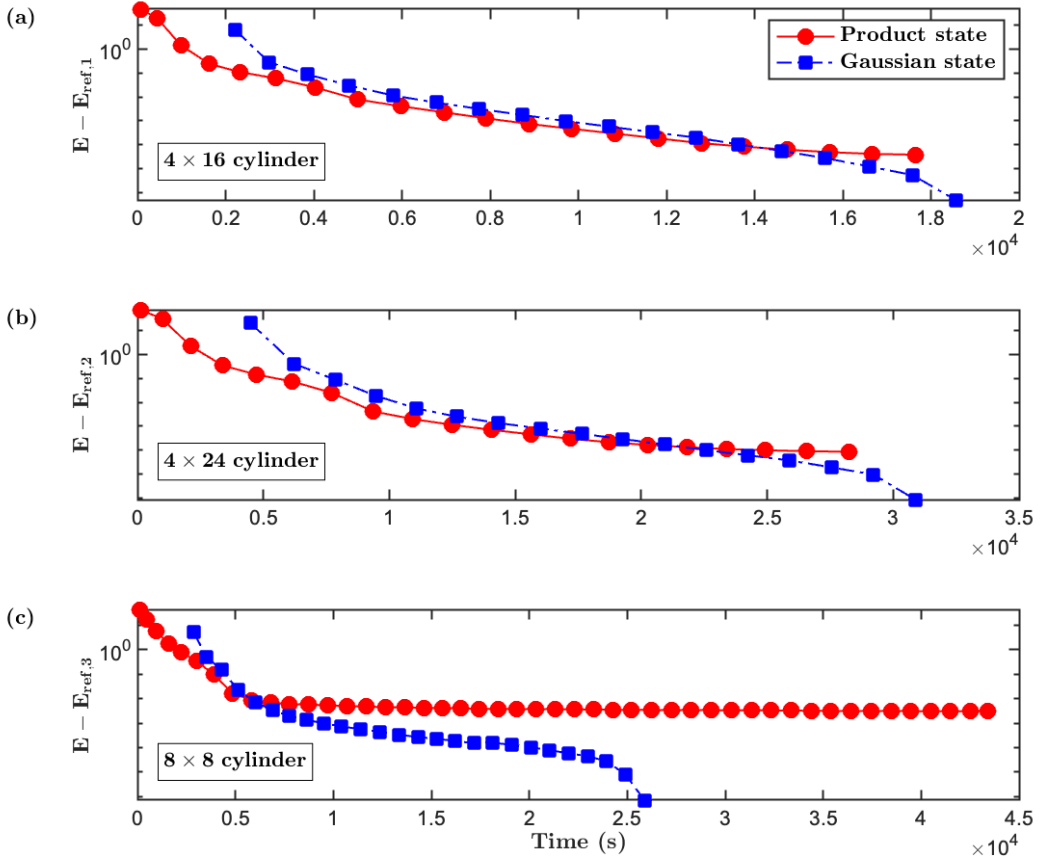


Figure 3.5.: Time evolution of the energy during the DMRG ground state search, initialized with a product state (red circles, solid line) and a Gaussian state (blue squares, dashed line). Each marker in the plot represents the energy after completing both a left-to-right and right-to-left sweep. Calculations were performed for the Hubbard model with parameters $t = 1$, $U = 5$ and $\mu = 0$ and a fixed maximum bond dimension $D = 1000$, for the following system sizes: (a) 4×16 cylinder, (b) 4×24 cylinder, (c) 8×8 cylinder. The first coordinate corresponds to the dimension with periodic boundary conditions. For (a) and (b), a two-site update protocol was used, while for (c) we used CBE DMRG. Since the true ground state energy is unknown, the energy is compared against a value $E_{ref,i}$ corresponding to the lowest energy between the product state and Gaussian state calculation minus the convergence criteria value.

convergence criteria, suggesting that the states may converge to different minima.

To better understand the converged states' differences in the 8×8 cylinder case, we plotted their spin distributions (Fig. 3.6). As predicted, the spin configurations in both cases correspond to an antiferromagnetic arrangement. The average local spin magnitude is nearly identical in both states, with the primary difference being that each state represents one of the two possible antiferromagnetic configurations.

Additionally, we repeated the DMRG calculations for the same configurations un-

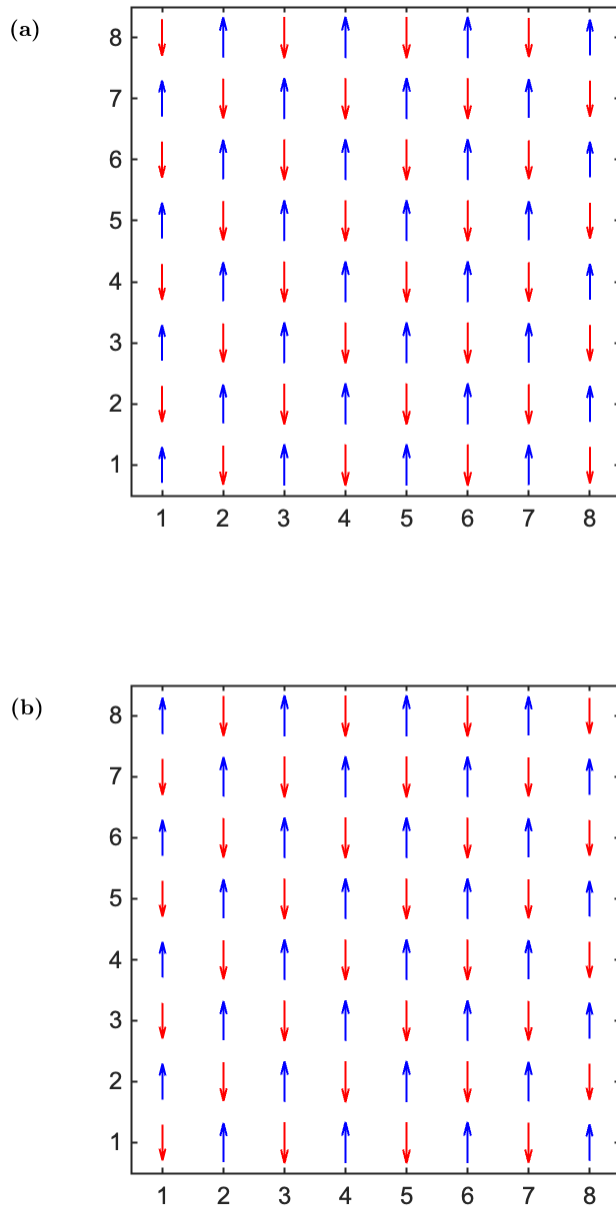


Figure 3.6.: Local spin distribution of the two converged states obtained through CBE DMRG in an 8×8 cylinder for Hubbard parameters $t = 1$, $U = 5$, and $\mu = 0$. Plot (a) corresponds to initializing DMRG with a product state, while (b) corresponds to the Gaussian state initialization. In both cases, the maximum bond dimension of the MPS was set to $D = 1000$. The size of the arrows is proportional to the spin magnitude.

der a more realistic scenario, where instead of maintaining a fixed bond dimension,

we allowed it to increase when a specific convergence criterion was met. The algorithm continues to increase the bond dimension until further increases no longer yield a significant reduction in the state energy (Fig. 3.7).

The Gaussian state still needs fewer sweeps to achieve convergence when allowing the bond dimension to adapt. However, when evaluating more relevant metrics, such as the computation time or the converged energy, the Gaussian state advantage vanishes. Further calculations for a different set of parameters showing a similar performance are shown in Fig. 3.8.

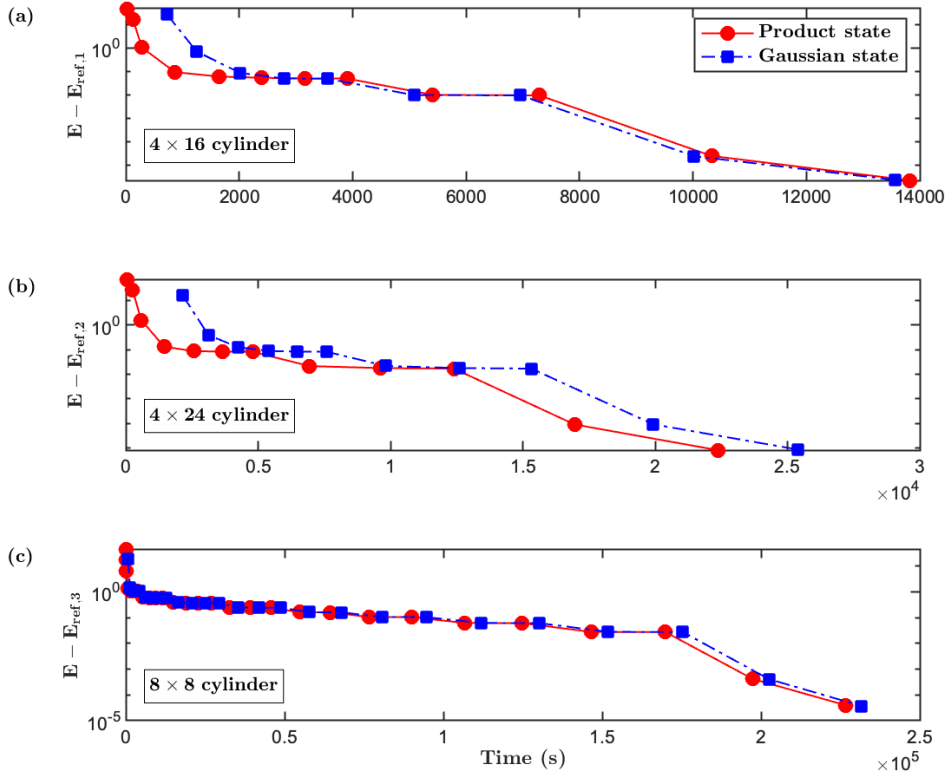


Figure 3.7.: Time evolution of the energy during the DMRG ground state search, initialized with a product state (red circles, solid line) and a Gaussian state (blue squares, dashed line). Each marker represents the energy after completing both a left-to-right and right-to-left sweep. Calculations were performed for the Hubbard model with parameters $t = 1$, $U = 5$ and $\mu = 0$, for the following system sizes: (a) 4×16 cylinder, (b) 4×24 cylinder and (c) 8×8 cylinder. The first coordinate corresponds to the dimension with periodic boundary conditions. The maximum bond dimension is allowed to increase when convergence is achieved, reaching values of (a) $D = 3000$, (b) $D = 3000$, and (c) $D = 9000$. For (a) and (b), a two-site update protocol was used, while for (c) we used CBE DMRG. Since the true ground state energy is unknown, the energy is compared against a value $E_{ref,i}$ corresponding to the lowest energy between the product state and Gaussian state calculation minus the convergence criteria value.

This behavior suggests that if we define a bond dimension D_{opt} such that it is sufficient to capture all the relevant physics of the ground state in an MPS for a given setting, and we set a maximum bond dimension D for our DMRG calculation, if the ratio D/D_{opt} is sufficiently large, the variational space of the product state becomes large enough to avoid the same local minima as the Gaussian state. As a result, both initial states may converge to the same final state, thereby nullifying the previously observed advantage of the Gaussian state.

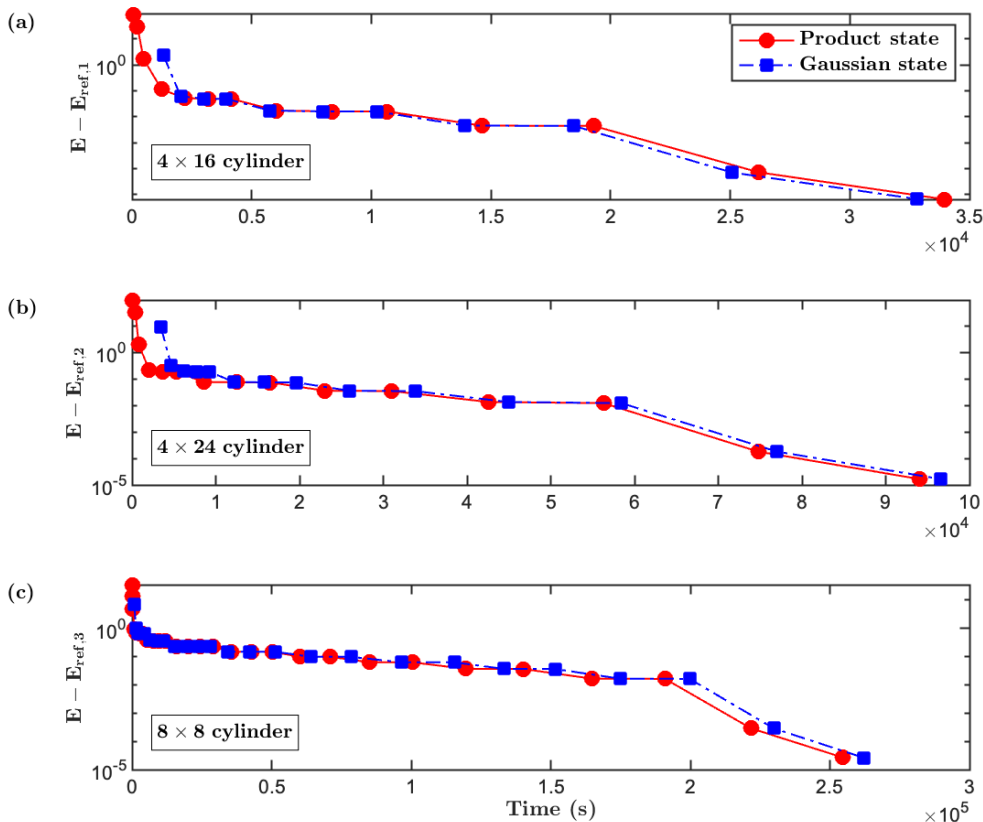


Figure 3.8.: Time evolution of the energy during the two-site DMRG ground state search, initialized with a product state (red circles, solid line) and a Gaussian state (blue squares, dashed line). Each marker represents the energy after completing both a left-to-right and right-to-left sweep. Calculations were performed for the Hubbard model with hopping parameter $t = 1$ and chemical potential $\mu = 0$, for the following system sizes and interaction terms: (a) 4×16 cylinder with $U = 1$, (b) 4×24 cylinder with $U = 3$, and (c) 8×8 cylinder with $U = 7$. The first coordinate corresponds to the dimension with periodic boundary conditions. The maximum bond dimension is allowed to increase when convergence is achieved, reaching values of (a) $D = 4000$, (b) $D = 5000$, and (c) $D = 9000$. Since the true ground state energy is unknown, the energy is compared against a value $E_{\text{ref},i}$ corresponding to the lowest energy between the product state and Gaussian state calculation minus the convergence criteria value.

3.2.2. Hole-doping case

In this section, we conduct a similar study for the 1/8-hole-doping case as the one performed previously. It is interesting to mention that since we are considering the Hubbard Hamiltonian as introduced in Eq. (1.1.4), the phase diagram of the model has a particle-hole symmetry and, therefore, it is enough for us to consider just the hole-doping case.

In principle, it is non-trivial to know beforehand the particle charge quantum number of the ground state when we move away from the half-filling setting. In our case, for a given set of Hubbard model parameters, we got the Gaussian state approximation to the ground state via imaginary time evolution as described in Sec. 2.1, analyzed its quantum numbers, and generated a product state which shares them. The initial product states used during our calculations for the 1/8-hole-doping case are shown in Fig. 3.9.

In the same way as in the half-filling scenario, we initially conducted a DMRG calculation with a fixed bond dimension of $D = 1000$ for two cylinders of sizes 4×16 and 4×24 . In both cases, we set the hopping parameter t as our energy scale, i.e., $t = 1$, and a fixed interaction $U = 1$ (Fig. 3.10). The exhibited behavior was similar to the one observed in the half-filling case, where the Gaussian state required fewer sweeps, achieved faster convergence, and reached a lower energy state than the product state. It is worth noting that the energy difference between the converged states for both cylinders is larger than in their corresponding half-filling settings, and so is the computation time advantage. However, this observation could be attributed to two factors. Firstly, based on the observed phenomenology in the half-filling case, the hole-doped ground state may have a larger optimal bond dimension

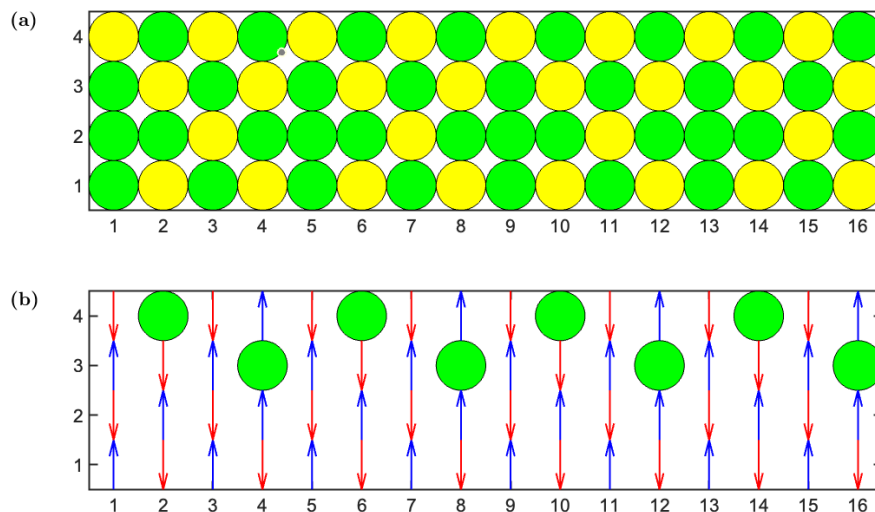


Figure 3.9.: Density and spin distributions of the initial product state for the (a) attractive and (b) repulsive cases in a 4×16 cylinder for a 1/8-hole-doped setting. Yellow circles represent particles, and green circles represent holes relative to the half-filling setting. The size of the circles and arrows is proportional to the magnitude of the corresponding quantities.

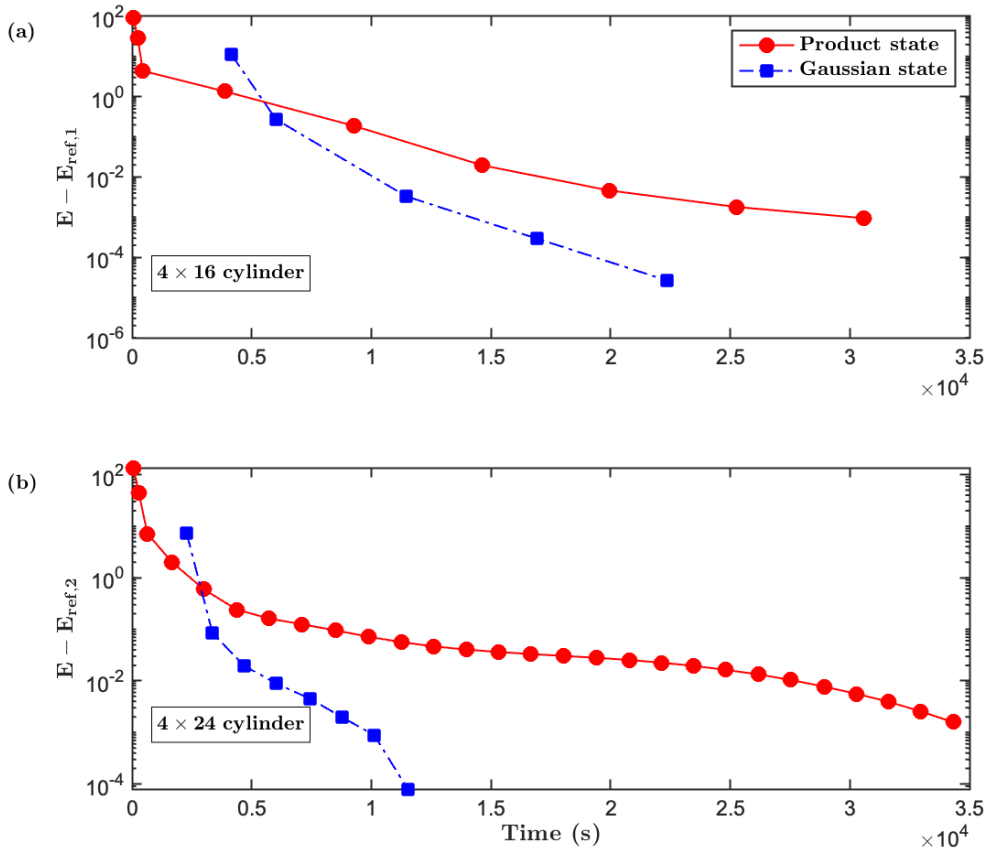


Figure 3.10.: Time evolution of the energy during the two-site DMRG ground state search, initialized with a product state (red circles, solid line) and a Gaussian state (blue squares, dashed line). Each marker represents the energy after completing both a left-to-right and right-to-left sweep. Calculations were performed for the Hubbard model with parameters $t = 1$, $U = 1$, and chemical potentials (a) $\mu = -0.3$ and (b) $\mu = -0.33$. The chemical potential values were chosen such that the particle density corresponds to a $1/8$ -hole-doping configuration. The maximum bond dimension is $D = 1000$, and the two cases correspond to (a) a 4×16 cylinder and (b) a 4×24 cylinder, where the first coordinate corresponds to the dimension with periodic boundary conditions. Since the true ground state energy is unknown, the energy is compared against a value $E_{\text{ref},i}$ corresponding to the lowest energy between the product state and Gaussian state calculation minus the convergence criteria value.

D_{opt} , which would reduce the ratio D/D_{opt} and therefore increase the advantage of the Gaussian state. Secondly, the interaction strength chosen here, $U = 1$, is smaller than in the previous case, reducing the influence of the quartic term in the Hubbard Hamiltonian relative to the quadratic terms, which suggests that the Gaussian state provides a better approximation to the true ground state.

We repeated the DMRG calculations but allowing to increase the bond dimension

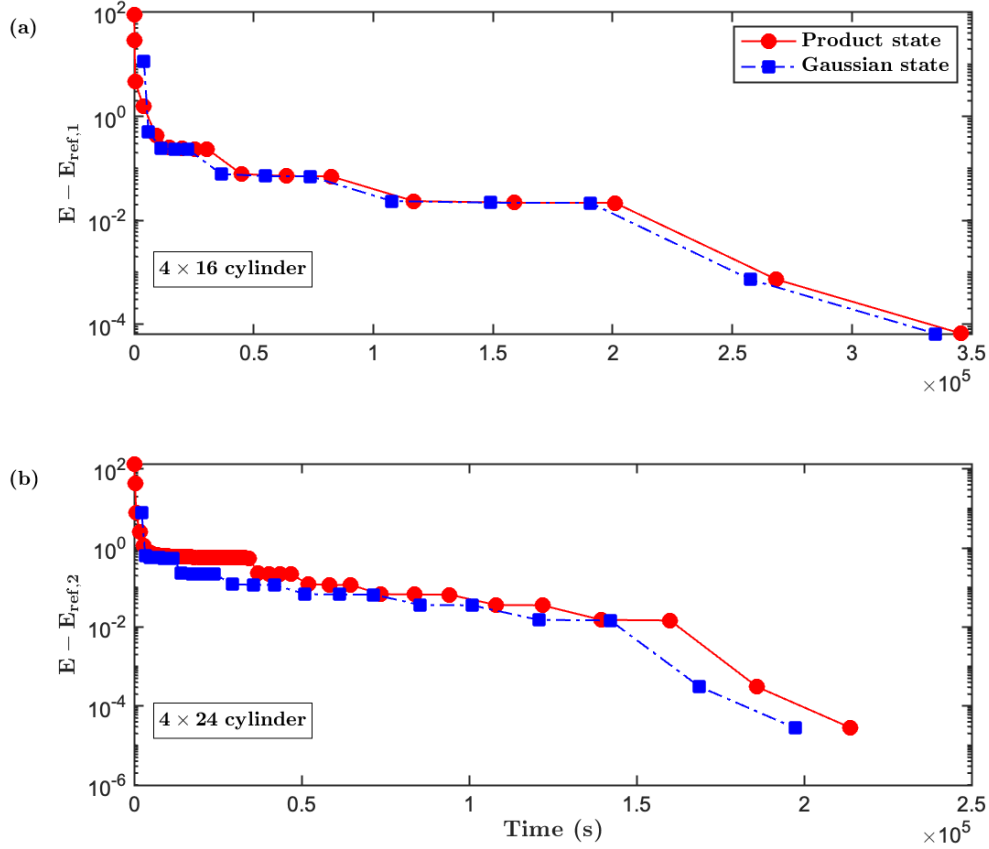


Figure 3.11.: Time evolution of the energy during the two-site DMRG ground state search, initialized with a product state (red circles, solid line) and a Gaussian state (blue squares, dashed line). Each marker represents the energy after completing both a left-to-right and right-to-left sweep. Calculations were performed for the Hubbard model with parameters $t = 1$, $U = 1$, and chemical potentials (a) $\mu = -0.3$ and (b) $\mu = -0.33$. The chemical potential values were chosen such that the particle density corresponds to a $1/8$ -hole-doping configuration. The maximum bond dimension is allowed to increase when convergence is achieved, reaching values of (a) $D = 4000$ and (b) $D = 7000$. The two cases correspond to (a) a 4×16 cylinder and (b) a 4×24 cylinder, where the first coordinate corresponds to the dimension with periodic boundary conditions. Since the true ground state energy is unknown, the energy is compared against a value $E_{\text{ref},i}$ corresponding to the lowest energy between the product state and Gaussian state calculation minus the convergence criteria value.

whenever convergence was achieved (Fig. 3.11). The results obtained are analogous to the half-filling setting: for a large enough bond dimension, the previously observed Gaussian state advantage vanishes.

Additionally, we examined the hole and spin distributions for the two converged states on the 4×16 cylinder with Hubbard parameters $t = 1$ and $U = 1$ (Fig. 3.12).

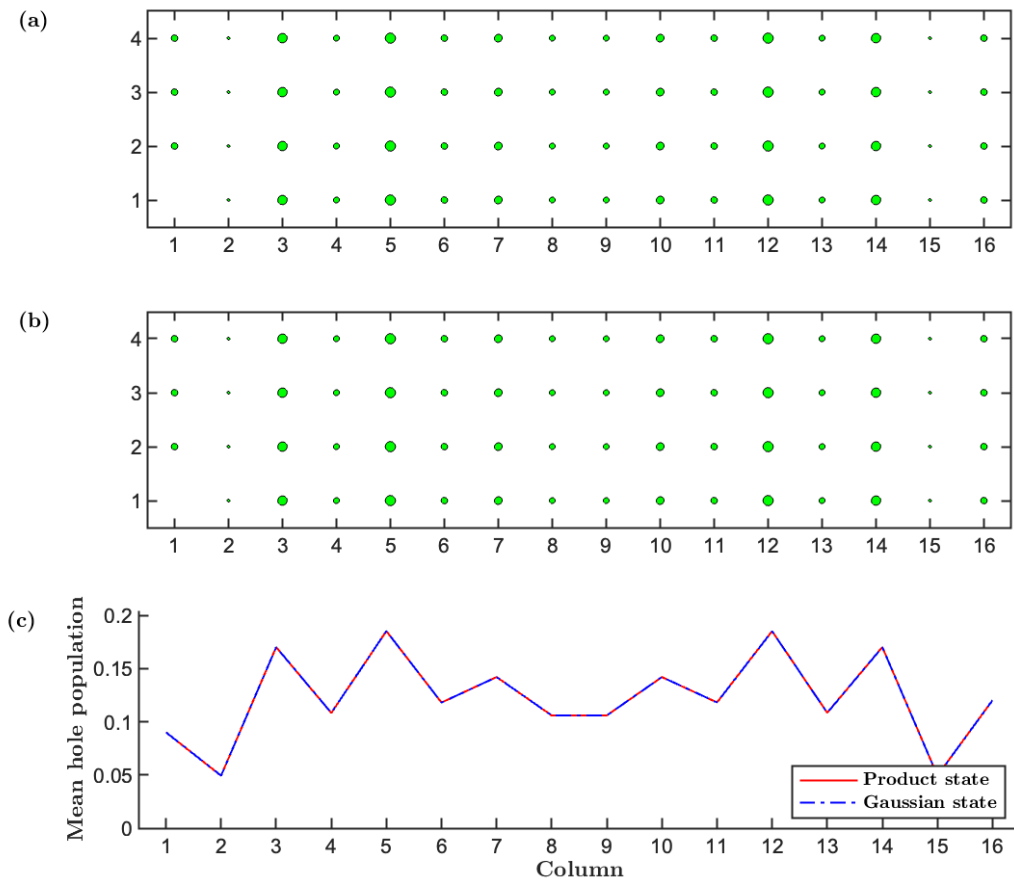


Figure 3.12.: Comparison of the local hole density relative to half-filling and spin distribution of the two converged states obtained through two-site DMRG in a 4×16 cylinder for Hubbard parameters $t = 1$, $U = 1$, and $\mu = -0.3$. The chemical potential value was chosen such that the particle density corresponds to a $1/8$ -hole-doping configuration. Plot (a) shows the hole and spin distribution of the converged state when initializing the DMRG calculation with a product state, while (b) corresponds to the Gaussian state initialization. Plot (c) compares the mean hole population per column of the two converged states. The MPS maximum bond dimension is $D = 4000$ for both cases. The circles and arrows sizes are proportional to the hole density and spin magnitudes, respectively.

Both initializations converge to nearly identical states, with their plotted distributions showing no noticeable differences. The hole density exhibits a fairly uniform pattern with no signs of stripe formation. Similarly, the spin distribution is also uniform, with magnitudes so close to zero that they are indistinguishable in the plot.

To conclude, we performed some additional computations on the 4×16 cylinder with different sets of parameters (Fig. 3.13). The results show that even though the behavior in the $U = 1$ case is similar to all the previously examined sets of

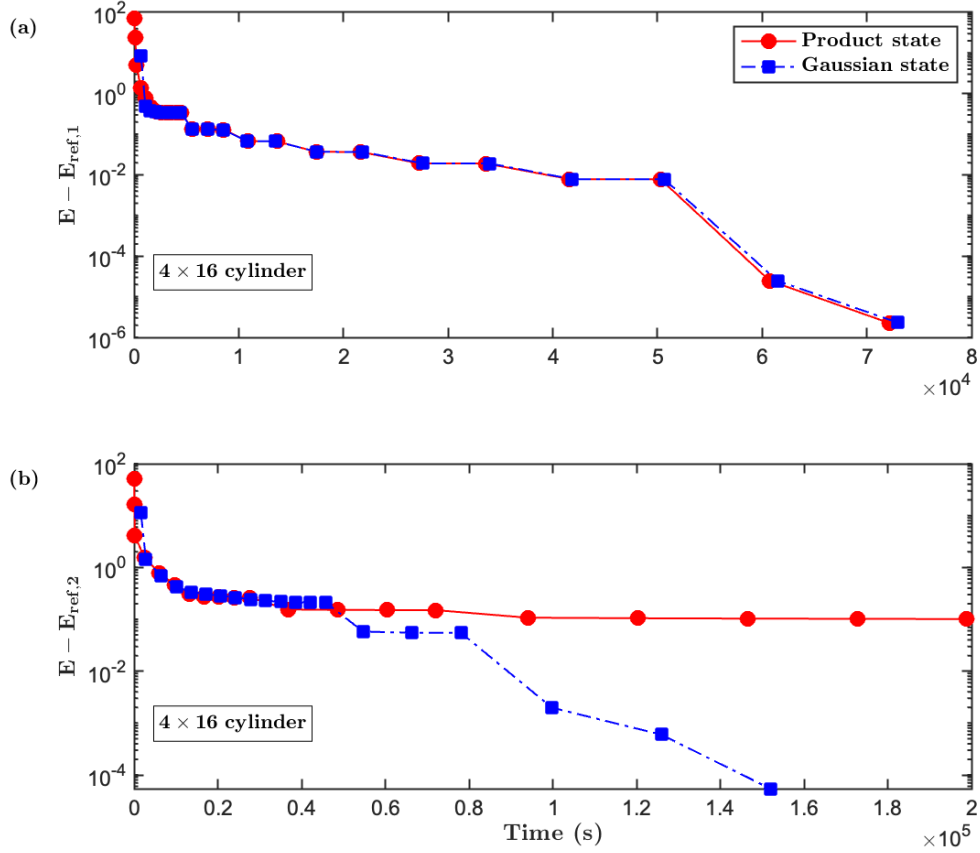


Figure 3.13.: Time evolution of the energy during the two-site DMRG ground state search, initialized with a product state (red circles, solid line) and a Gaussian state (blue squares, dashed line). Each marker represents the energy after completing both a left-to-right and right-to-left sweep. The lattice is set on a 4×16 cylinder, where the first coordinate corresponds to the dimension with periodic boundary conditions. Calculations were performed for the Hubbard model with (a) hopping term $t = 1$, interaction term $U = 3$ and chemical potential $\mu = -0.6$, and (b) hopping term $t = 1$, interaction term $U = 7$ and chemical potential $\mu = -1.8396$. The chemical potential values were chosen such that the particle density corresponds to a $1/8$ -hole-doping configuration. The maximum bond dimension is allowed to increase when convergence is achieved, reaching values of (a) $D = 7000$ and (b) $D = 3000$. Since the true ground state energy is unknown, the energy is compared against a value $E_{ref,i}$ corresponding to the lowest energy between the product state and Gaussian state calculation minus the convergence criteria value.

parameters, in the $U = 7$ case, the fermionic Gaussian state clearly outperforms its counterpart. This result indicates that, for this configuration, initializing DMRG with a Gaussian state MPS allows us to circumvent a local minimum in which our product state would get stuck. That behavior was not expected since it is the only set of parameters for which such a clear advantage was observed for a reasonable bond

dimension. Additionally, it corresponds to a case where the interaction strength U is the largest among all the previously studied, suggesting that the initial fermionic Gaussian state approximation should be further from the true ground state.

To gain a clearer understanding of the characteristics of each converged state in the $U = 7$ case, we compared their local hole and spin distributions (Fig. 3.14). In this case, the two states display distinct patterns. The state resulting from the product state initialization shows a more dispersed hole distribution, with most of the holes concentrated near the center of the cylinder. Its spin distribution is also more uniform, exhibiting a consistent antiferromagnetic pattern. In contrast, the state obtained from the Gaussian state displays two distinct stripes in the hole distribution, acting as domain walls for the spin configuration. This results in an antiferromagnetic pattern in the center of the cylinder and a reversed configuration at the edges.

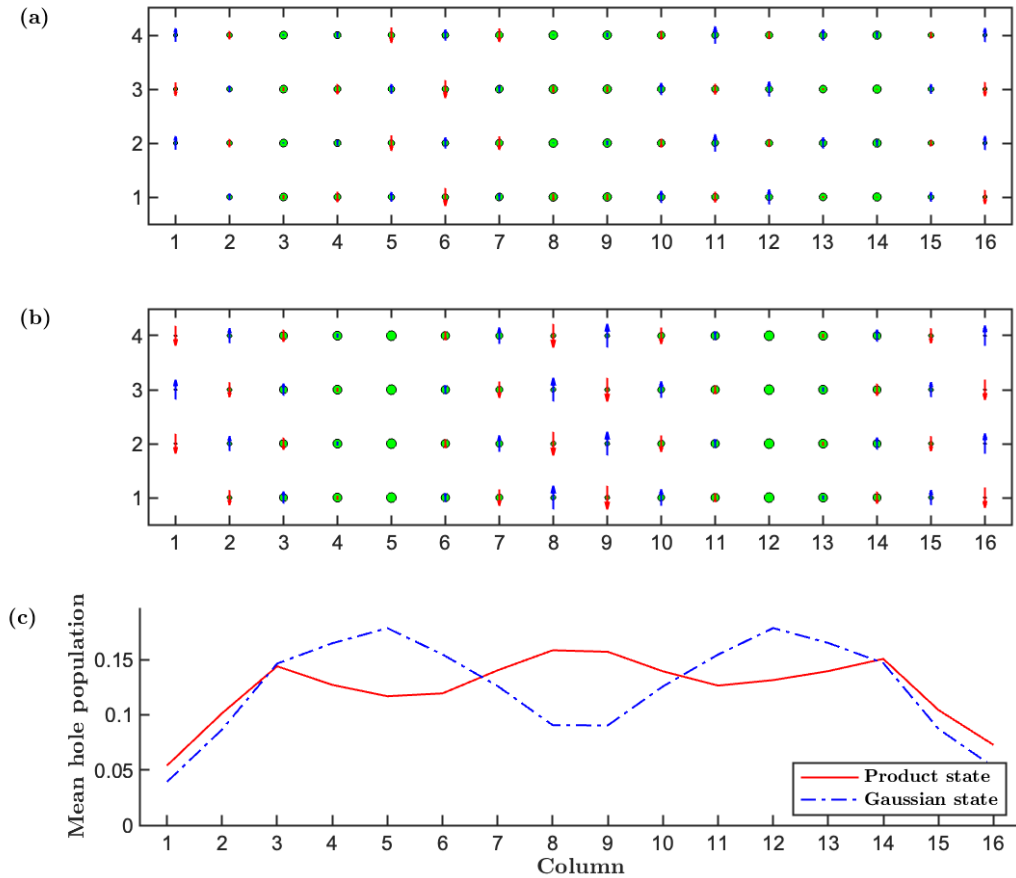


Figure 3.14.: Comparison of the local hole density relative to half-filling and spin distribution of the two converged states obtained through two-site DMRG in a 4×16 cylinder for Hubbard parameters $t = 1$, $U = 7$, and $\mu = -1.8396$. The chemical potential value was chosen such that the particle density corresponds to a $1/8$ hole doping configuration. Plot (a) shows the hole and spin distribution of the converged state when initializing the DMRG calculation with a product state, while (b) corresponds to the Gaussian state initialization. Plot (c) compares the mean hole population per column of the two converged states. The MPS maximum bond dimension is $D = 3000$ for both cases. The circles and arrows sizes are proportional to the hole density and spin magnitudes, respectively.

4. Summary and outlook

Summary. In this thesis, we have assessed the efficiency of utilizing a Gaussian state as the initial ansatz for performing DMRG calculations on the 2D Hubbard model. We successfully implemented an algorithm that computes a fermionic Gaussian state approximation to the real ground state through imaginary time evolution, subsequently compresses into its MPS form and uses it as the initial ansatz for a DMRG calculation.

A comparison between the efficiency of using the Gaussian state and a product state as initial ansatz was conducted, as detailed in Chapter 3. This comparison focused on both the half-filling and 1/8-hole-doping cases, with the primary metrics being the computational time required and the energy of the converged state.

The results indicate that while the Gaussian state performs better with a low maximum bond dimension, it does not generally outperform the product state when a reasonable maximum bond dimension is used in DMRG calculations. However, we found an exception in one of the 1/8-hole-doping cases, where the Gaussian state converges to a lower energy state, highlighting its potential advantages in specific situations. Furthermore, the Gaussian state approximation can be particularly useful in studying the Hubbard model under conditions where determining the quantum numbers of the ground state is difficult, as it automatically provides a reasonable initial guess for them.

Outlook. This thesis has provided an initial study on the usage of fermionic Gaussian states as the initial ansatz for DMRG calculations when studying Hubbard-like models. Some proposed further research directions are:

- Even though the Gaussian state has not generally shown a relevant advantage for the considered Hubbard model, it could be interesting to study the performance when adding an extra next-to-nearest-neighbor hopping term. The Hubbard model with that extra term has been of interest since some numerical studies show that it can enhance superconductivity [33–35]. The next-to-nearest-neighbor hopping term involves a longer range hopping, which implies an increment in the MPO’s bond dimension and, consequently, a more expensive DMRG calculation. Under such circumstances, a possible Gaussian state advantage could be more relevant.
- When compressing the Gaussian state into an MPS, some of the information of the state is lost. Additionally, the MPS conversion requires considerably more computational time than the obtention of the covariance matrix describing the state. A recent study has proposed a more efficient MPS conversion of particle-number conserving fermionic Gaussian states [36]. Implementing this method in our algorithm may lead to better performance.
- The method could be more useful for the study of models for which little information about the true ground state is available. Although this thesis

focused on the study of the Hubbard model, any Hamiltonian that can be brought to the form shown in Eq. 2.1.1 is suitable for being studied through this method. Some Hamiltonians which can be of special interest are the so-called all-to-all interactions Hamiltonians, which are specially popular in quantum chemistry.

- Mean-field theories are widely employed in condensed matter physics to provide an analytical approximation of a model's ground state. These techniques involve replacing the complex many-body interactions with a mean field plus a quantum fluctuation, while neglecting second-order quantum fluctuations. This approach effectively transforms the Hamiltonian into a quadratic form, which can then be analytically solved to obtain the so-called mean-field solution. Since the ground state of a quadratic Hamiltonian is a fermionic Gaussian state, the Gaussian state used to initialize our DMRG calculation should be at least as accurate as the best possible mean-field approximation. Analyzing the relationship between the initial Gaussian state and the DMRG-converged state could provide valuable insights into the accuracy of mean-field approximations.

A. Numerical implementation of the Bloch-Messiah decomposition

The MPS conversion of a Gaussian state using the Pfaffian overlap method introduced in Sec. 2.2.2 can be highly sensitive to numerical errors. This issue is particularly significant in the implementation outlined in this thesis, where the covariance matrix is obtained numerically and already carries its inherent errors. If not handled carefully, the accumulation of these errors can result in the matrix from Eq. (2.2.29) losing its antisymmetric property, making it impossible to compute the Pfaffian and causing the method to fail.

In our experience, performing an accurate Bloch-Messiah decomposition is the most critical and sensitive step for a successful implementation. In this appendix, we present the Bloch-Messiah decomposition algorithm that has yielded the best results in our work:

1. Obtain the Bogoliubov matrix. We do it by getting the unitary transformation B'_A that diagonalizes the reduced covariance matrix. Since the columns of B'_A represent eigenmodes, there is a global phase freedom that could prevent it from having the exact shape introduced in Eq. (2.2.14). To solve it, we identify the upper-left and lower-left blocks of B'_A with U_A and V_A , respectively. Afterward, we define our Bogoliubov transformation as

$$B_A = \begin{pmatrix} U_A & V_A^* \\ V_A & U_A^* \end{pmatrix} \quad (\text{A.0.1})$$

2. Now that we have identified U_A and V_A , we can begin with the proper Bloch-Messiah decomposition. First, we realize that U_A is decomposed as $U_A = D_A \bar{U}_A C_A$ with D_A and C_A being unitary matrices and \bar{U}_A being a diagonal matrix. Therefore, we can obtain a first guess of these matrices by performing an SVD decomposition $U_A = USV^\dagger$ and identifying $D'_A = U$, $\bar{U}'_A = S$ and $C'_A = V^\dagger$.
3. Identify which diagonal values correspond to occupied, paired, and empty modes. Theoretically, the occupied modes correspond to the diagonal values of \bar{U}_A that are equal to 0, the empty modes correspond to the diagonal values of \bar{U}_A that are equal to 1 and the paired modes are the rest. However, determining them in the presence of numerical errors is not that straightforward.

In our case, we start by generating 5 sets of modes: the definitely occupied O' , paired P' , and empty E' ; and the suspicious to be occupied O^{sus} , and empty E^{sus} . If we denote the elements of \bar{U}'_A as $[\bar{U}'_A]_{kl} = u_k \delta_{kl}$, we define each set as

- $O' = \{u_k \mid u_k < 10^{-10}\}$
- $O^{sus} = \{u_k \mid 10^{-10} < u_k < 0.1\}$

- $P' = \{u_k \mid 0.1 < u_k < 0.9\}$
- $E^{sus} = \{u_k \mid 0.9 < u_k < 1 - 10^{-10}\}$
- $E' = \{u_k \mid 1 - 10^{-10} < u_k\}$

From those 5 sets, we can generate our sets of occupied O , paired P and E modes as

- $O = O' \cup \{u_k \in O^{sus} \mid \nexists u_l \in O^{sus}, |u_k - u_l| < 10^{-8} \text{ for } k \neq l\}$
- $P = P' \cup \{u_k, u_l \in O^{sus} \cup E^{sus} \mid |u_k - u_l| < 10^{-8}\}$
- $E = E' \cup \{u_k \in E^{sus} \mid \nexists u_l \in E^{sus}, |u_k - u_l| < 10^{-8} \text{ for } k \neq l\}$

4. Identify values u_p from Eq. (2.222). We do so by sorting the values in P in descending order and selecting the ones in odd positions.
5. Build matrix \bar{U}_A . If we denote the number of occupied modes as N_O , the number of empty modes as N_E and the number of u_p values as N_P , we can define \bar{U}_A as

$$U_A = \mathbb{1}_{N_E \times N_E} \oplus \bigoplus_{p=1}^{N_P} u_p \sigma^0 \oplus \mathbb{0}_{N_O \times N_O}, \quad (\text{A.0.2})$$

with σ^0 the 2×2 identity matrix.

6. Get values v_p . We obtain them from u_p as $v_p = \sqrt{1 - u_p^2}$.
7. Build matrix \bar{V}_A as

$$V_A = \mathbb{0}_{N_E \times N_E} \oplus \bigoplus_{p=1}^{N_P} i v_p \sigma^y \oplus \mathbb{1}_{N_O \times N_O}, \quad (\text{A.0.3})$$

where σ^y is the 2×2 Pauli-Y matrix.

8. Obtain matrices D_A and C_A . Due to the global phase freedom, matrices D'_A and C'_A define a matrix $\bar{V}'_A = D'^T_A V_A C'_A \neq \bar{V}_A$. The difference between \bar{V}'_A and \bar{V}_A is that the elements of \bar{V}'_A are not necessarily real and have arbitrary complex phases. If \bar{V}_A is a $N \times N$ matrix, we get rid of the complex phases of \bar{V}'_A as follows:

- For all $k = 1, 2, \dots, N$ such that $[\bar{V}_A]_{kk} \neq 0$ (i.e., the occupied eigenmodes), we multiply the k -th column of D'_A by $e^{-i\phi_k}$ with ϕ_k the phase such that $[\bar{V}'_A]_{kk} = e^{i\phi_k}$.
- For all $k = 1, 2, \dots, N$ such that $[\bar{V}_A]_{kk} = 0$ and $[\bar{V}_A]_{k,k+1} \neq 0$ (i.e., the paired eigenmodes), we multiply the k -th column of D'_A by $e^{-i\phi_k}$ and the k -th row of C'_A by $e^{i\phi_k}$ with ϕ_k the phase such that $[\bar{V}'_A]_{k,k+1} = v_p e^{i\phi_k}$ for $p = (k - N_E + 1)/2$.

After that, we have successfully transformed $D'_A \rightarrow D_A$ and $C'_A \rightarrow C_A$, such that $U_A = D_A \bar{U}_A C_A$ and $V_A = D_A^* \bar{V}_A C_A$.

Bibliography

- [1] Steven R. White. Density matrix formulation for quantum renormalization groups. Phys. Rev. Lett., 69:2863–2866, Nov 1992.
- [2] Steven R. White. Density matrix renormalization group algorithms with a single center site. Phys. Rev. B, 72(18), Nov 2005.
- [3] Ian P. McCulloch. From density-matrix renormalization group to matrix product states. J. Stat. Mech., 2007(10):P10014, Oct 2007.
- [4] C. Hubig, Ian P. McCulloch, U. Schollwock, and Fred A. Wolf. Strictly single-site dmrg algorithm with subspace expansion. Phys. Rev. B, 91:155115, Apr 2015.
- [5] Andreas Gleis, Jheng-Wei Li, and Jan von Delft. Projector formalism for kept and discarded spaces of matrix product states. Phys. Rev. B, 106(19):195138, Nov 2022.
- [6] Hui-Ke Jin, Hong-Hao Tu, and Yi Zhou. Density matrix renormalization group boosted by gutzwiller projected wave functions. Phys. Rev. B, 104(2):L020409, Jul 2021.
- [7] Ji-Yao Chen, Jheng-Wei Li, Pierre Nataf, Sylvain Capponi, Matthieu Mambrini, Keisuke Totsuka, Hong-Hao Tu, Andreas Weichselbaum, Jan von Delft, and Didier Poilblanc. Abelian $su(n)_1$ chiral spin liquids on the square lattice. Phys. Rev. B, 104(23):235104, Dec 2021.
- [8] Hui-Ke Jin, Rong-Yang Sun, Hong-Hao Tu, and Yi Zhou. Unveiling a critical stripy state in the triangular-lattice $su(4)$ spin-orbital model. Sci. Bull., 67(9):918–917, May 2022.
- [9] Rong-Yang Sun, Hui-Ke Jin, Hong-Hao Tu, and Yi Zhou. Possible chiral spin liquid state in the $s=1/2$ kagome heisenberg model. npj Quantum Materials, 9(1):16, Feb 2024.
- [10] Hui-Ke Jin, W. M. H. Natori, and Johannes Knolle. Twisting the dirac cones of the $su(4)$ spin-orbital liquid on the honeycomb lattice. Phys. Rev. B, 107(18):L180401, May 2023.
- [11] Sergey Bravyi. Lagrangian representation for fermionic linear optics, 2004. arXiv:quant-ph/0404180.
- [12] Jacopo Surace and Luca Tagliacozzo. Fermionic Gaussian states: an introduction to numerical approaches. SciPost Phys. Lect. Notes, page 54, 2022.

- [13] Christina V Kraus and J Ignacio Cirac. Generalized hartree–fock theory for interacting fermions in lattices: numerical methods. New J. Phys., 12(11):113004, nov 2010.
- [14] John Hubbard. Electron correlations in narrow energy bands. R. Soc., 281:401–419, 1963.
- [15] Antoine Georges, Gabriel Kotliar, Werner Krauth, and Marcelo J. Rozenberg. Dynamical mean-field theory of strongly correlated fermion systems and the limit of infinite dimensions. Rev. Mod. Phys., 68:13–125, Jan 1996.
- [16] Andrea C. Cosentini, Massimo Capone, Leonardo Guidoni, and Giovanni B. Bachelet. Phase separation in the two-dimensional hubbard model: A fixed-node quantum monte carlo study. Phys. Rev. B, 58:R14685–R14688, Dec 1998.
- [17] Luca F. Tocchio, Federico Becca, Alberto Parola, and Sandro Sorella. Role of backflow correlations for the nonmagnetic phase of the $t-t'$ hubbard model. Phys. Rev. B, 78:041101, Jul 2008.
- [18] Steven R. White and Douglas J. Scalapino. Stripes on a 6-leg hubbard ladder. Phys. Rev. Lett., 91:136403, Sep 2003.
- [19] Mattias H. Hettler, M. Mukherjee, Mark Jarrell, and Hulikal R. Krishnamurthy. Dynamical cluster approximation: Nonlocal dynamics of correlated electron systems. Phys. Rev. B, 61:12739–12756, May 2000.
- [20] Gabriel Kotliar, Sergej Y. Savrasov, Gunnar Pálsson, and Giulio Biroli. Cellular dynamical mean field approach to strongly correlated systems. Phys. Rev. Lett., 87:186401, Oct 2001.
- [21] Bo-Xiao Zheng and Garnet Kin-Lic Chan. Ground-state phase diagram of the square lattice hubbard model from density matrix embedding theory. Phys. Rev. B, 93(3), Jan 2016.
- [22] Douglas J. Scalapino. Numerical studies of the 2d hubbard model, 2006. arXiv:cond-mat/0610710.
- [23] Hans-Peter Eckle. Models of Strongly Interacting Quantum Matter. In Models of Quantum Matter: A First Course on Integrability and the Bethe Ansatz, chapter 8, pages 241–420. Oxford University Press, 07 2019.
- [24] Thierry Giamarchi. Interacting Fermions in a Lattice. In Quantum Physics in One Dimension, chapter 7, pages 200–237. Oxford University Press, 12 2003.
- [25] Corneliu Lanczos. An iteration method for the solution of the eigenvalue problem of linear differential and integral operators. J. Res. Nat. Bur. Stand., 45, Oct 1950.
- [26] Volker Bach, Elliott H. Lieb, and Jan Philip Solovej. Generalized hartree-fock theory and the hubbard model. J. Stat. Phys., 76:3–89, 1994.
- [27] S. Kivelson. Wannier functions in one-dimensional disordered systems: Application to fractionally charged solitons. Phys. Rev. B, 26:4269–4277, Oct 1982.

- [28] Ying-Hai Wu, Lei Wang, and Hong-Hao Tu. Tensor network representations of parton wave functions. Phys. Rev. Lett., 124:246401, Jun 2020.
- [29] Hui-Ke Jin, Rong-Yang Sun, Yi Zhou, and Hong-Hao Tu. Matrix product states for hartree-fock-bogoliubov wave functions. Phys. Rev. B, 105:L081101, Feb 2022.
- [30] Claude Bloch and Albert Messiah. The canonical form of an antisymmetric tensor and its application to the theory of superconductivity. Nucl. Phys., 39:95–106, 1962.
- [31] Peter Ring and Peter Schuck. The Nuclear Many-Body Problem. Springer Berlin, Heidelberg, 1980.
- [32] George F. Bertsch and Luis M. Robledo. Symmetry restoration in hartree-fock-bogoliubov based theories. Phys. Rev. Lett., 108:042505, Jan 2012.
- [33] Boris Ponsioen, Sangwoo S. Chung, and Philippe Corboz. Period 4 stripe in the extended two-dimensional hubbard model. Phys. Rev. B, 100:195141, Nov 2019.
- [34] Yi-Fan Jiang, Jan Zaanen, Thomas P. Devereaux, and Hong-Chen Jiang. Ground state phase diagram of the doped hubbard model on the four-leg cylinder. Phys. Rev. Research, 2(3):033073, Jul 2020.
- [35] Chia-Min Chung, Mingpu Qin, Shiwei Zhang, Ulrich Schollwöck, and Steven R. White. Plaquette versus ordinary d -wave pairing in the t' -hubbard model on a width-4 cylinder. Phys. Rev. B, 102:041106, Jul 2020.
- [36] Tong Liu, Ying-Hai Wu, Hong-Hao Tu, and Tao Xiang. Efficient conversion from fermionic gaussian states to matrix product states, 2024. arXiv:2408.01155.